Drug Design, Development and Therapy

Dovepress
Taylor & Francis Group

Open Access Full Text Article

ORIGINAL RESEARCH

Integrated Serum Pharmacochemistry, Network Pharmacology, and Transcriptomics Reveal the Mechanisms and Active Constituents of Qingfei Huoxue Decoction Against Bleomycin-Induced Pulmonary Fibrosis

Yule Wang[1–3,*], Juntao Wang[4,*], Ruiling Lu[1,*], Yan Zhu[5], Bei Li[1–3,*], Yue Gao[1–3]

[1]The Fourth School of Clinical Medicine, Zhejiang Chinese Medical University, Hangzhou First People's Hospital, Hangzhou, People's Republic of China; [2]Zhejiang Key Laboratory of Traditional Chinese Medicine for the Prevention and Treatment of Senile Chronic Diseases, Affiliated Hangzhou First People's Hospital, School of Medicine, Westlake University, Hangzhou, People's Republic of China; [3]Department of Geriatrics, Affiliated Hangzhou First People's Hospital, School of Medicine, Westlake University, Hangzhou, People's Republic of China; [4]Pharmaceutical Informatics Institute, College of Pharmaceutical Sciences, Zhejiang University, Hangzhou, People's Republic of China; [5]State Key Laboratory of Component-based Chinese Medicine, Tianjin University of Traditional Chinese Medicine, Tianjin, People's Republic of China

*These authors contributed equally to this work

Correspondence: Yue Gao; Yan Zhu, Email gaoyue@hospital.westlake.edu.cn; yanzhu.harvard@icloud.com

Background: Pulmonary fibrosis (PF) is a progressive and fatal interstitial lung disorder with limited therapeutic options, as current drugs like pirfenidone and nintedanib offer only modest benefits and carry adverse events. Given the lung-protective and anti-inflammatory activities of Qingfei Huoxue decoction (QFHXD), its anti-PF efficacy, pharmacological mechanisms, and active constituents warrant further investigation.

Methods: A bleomycin (BLM)-induced PF mouse model was used to assess QFHXD's efficacy. The bioactive components of QFHXD and their distribution in lung tissue were identified in vivo through serum pharmacochemistry. An integrative approach combining network pharmacology, transcriptomics, and molecular validation was employed to elucidate the QFHXD's therapeutic mechanisms. The anti-PF active substances were defined by cellular immunofluorescence and molecular docking.

Results: Treatment with QFHXD effectively preserved alveolar integrity, suppressed inflammation, reduced expression of pro-fibrotic markers, and decreased extracellular matrix deposition, thereby improving histopathology and survival in PF mice. Serum pharmacochemistry identified 46 QFHXD absorbable and lung-distributed compounds. Integrated component-target-disease network and transcriptome analyses revealed a central role of anti-inflammation and anti-apoptosis for QFHXD against PF. Indeed, QFHXD inhibited the overexpression of pivotal inflammatory mediators TLR2, TLR4, NF-κB, IL-1β, IL-6, TNF-α, TGF-β1, CCL2, SPP1, and MMP9 in fibrotic lung tissues. QFHXD also ameliorated the apoptotic phenotype and reduced the dysregulated levels of Bcl2, Bax, and Caspase-3 expression. QFHXD and several of its active components normalized pro-fibrotic markers Fibronectin and Collagen I in TGF-β1-stimulated MRC-5 cells, an effect mediated by their multi-target binding to key PF-related proteins (TGF-β1, TLR4, CCL2, SPP1, MMP9, and Caspase-3), as supported by molecular docking.

Conclusion: Our findings demonstrated a potent anti-PF efficacy of QFHXD, attributed at least in part to its multi-targeted anti-inflammatory and anti-apoptotic activities. Loganin, baicalein, baicalin, oroxylin A, peimine, peiminine, tanshinone IIA, nobiletin, and paeoniflorin were identified as the primary active components of QFHXD against PF.

Keywords: bleomycin-induced pulmonary fibrosis, Qingfei Huoxue decoction, serum pharmacochemistry, network pharmacology, transcriptome sequencing, inflammatory and apoptotic regulatory mechanisms, active constituents

https://doi.org/10.2147/DDDT.S592770
Received: 20 January 2026
Accepted: 31 March 2026
Published: 7 April 2026

Graphical Abstract

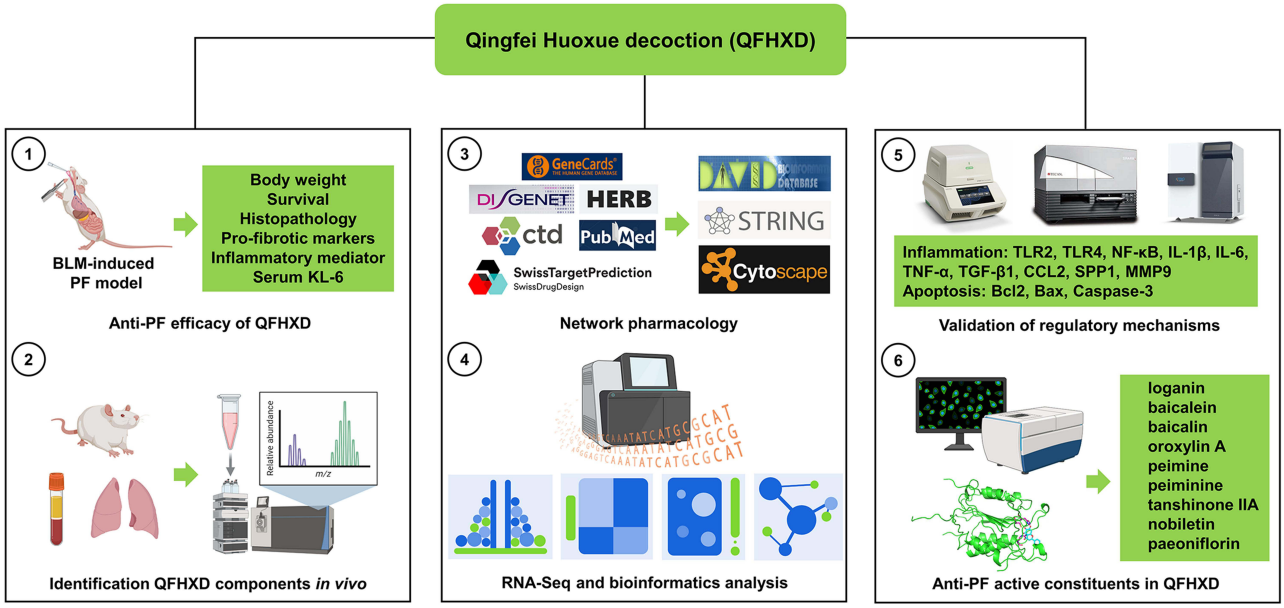

Introduction

Pulmonary fibrosis (PF) is a chronic, progressive interstitial lung disease of unknown etiology and has become a global public health issue with considerable morbidity and mortality, along with a substantial socio-economic burden.[1,2] It is characterized by abnormal repair of damaged alveolar epithelium, infiltration of inflammatory cells, excessive proliferation of fibroblasts and myofibroblasts, and pathologic accumulation of extracellular matrix (ECM), which collectively drive adverse lung remodeling and poor outcomes (eg, deteriorative lung function, respiratory failure, and even death).[3,4] Notably, the Coronavirus Disease 2019 (COVID-19) pandemic has heightened global concerns about PF, as Severe Acute Respiratory Syndrome Coronavirus 2 (SARS-CoV-2) infection can trigger fibrotic phenotypes (eg, alveolar epithelial damage, inflammatory reaction, and proliferation of fibroblasts) that lead to post-COVID-19 lung fibrosis.[5,6] Currently, pirfenidone, nintedanib, and nerandomilast are the only three pharmacotherapies approved by the United States Food and Drug Administration (FDA) for PF treatment.[7] Although they have proven efficacy in decelerating disease progression, maintaining lung function, and improving clinical outcomes, their use is limited by adverse events such as gastrointestinal disorders, cardiovascular events, and weight loss.[8,9] In addition, non-pharmacological interventions (eg, pulmonary rehabilitation, lung transplantation, and palliative care) contribute to symptomatic relief and improvement of living quality.[10] However, lung transplantation is only available for specific patients. Therefore, exploiting alternative options for PF treatment is urgently needed.

Using Traditional Chinese Medicine (TCM) in preventing and treating PF has been documented.[11,12] TCM theory classifies PF as lung atrophy and lung impediment, with primary causes including fire-heat, phlegm stagnation, Qi deficiency, and blood stasis.[13] Guided by the TCM principle of syndrome differentiation and treatment, TCM prescriptions, consisting of multiple Chinese medicinal herbs (CMHs) in appropriate proportions, can work synergistically to fight PF through pathways such as clearing heat, detoxification, expelling phlegm, regulating Qi, activating blood, and removing stasis.[14] Qingfei Huoxue decoction (QFHXD), which includes *Lonicera japonica* Thunb. (Jinyinhua), *Forsythia suspensa* (Thunb). Vahl (Lianqiao), *Scutellaria baicalensis* Georgi (Huangqin), *Taraxacum mongolicum* Hand.-Mazz. (Pugongying), *Fritillaria thunbergii* Miq. (Zhebeimu), *Angelica sinensis* (Oliv). Diels (Danggui), *Salvia miltiorrhiza* Bunge (Danshen), *Citrus reticulata* Blanco (Chenpi), *Coix lacryma-jobi var. ma-yuen* (Rom. Caill). Stapf (Yiyiren), *Paeonia lactiflora* Pall. (Baishao), *Bupleurum chinense* DC. (Chaihu), *Aesculus chinensis* Bunge (Suoluoguo), *Curcuma wenyujin* Y.H.Chen & C.Ling (Yujin), *Cyperus rotundus* L. (Xiangfu), *Perilla frutescens* (L). Britton (Zisugeng), *Peucedanum praeruptorum* Dunn (Qianhu), *Prunus*

mandshurica (Maxim). Koehne (Kuxingren), and *Platycodon grandiflorus* (Jacq). A. DC. (Jiegeng), is an effective prescription medicine for treating respiratory diseases.[15]

The accumulating pharmacological evidence indicated that anti-PF properties of heat-clearing and detoxifying TCMs, such as Jinyinhua and Huangqin, were relevant to the modulation of anti-inflammatory, anti-oxidative, and anti-apoptotic mechanisms.[16,17] CMHs used for eliminating phlegm, such as Chenpi and Jiegeng, exerted beneficial effects against PF via anti-inflammation and anti-apoptosis.[18,19] Additionally, Chenpi, known for its Qi-regulating function, could also resist oxidation and suppress fibroblast activation to prevent PF.[20] As the frequently used CMHs for blood-activating and stasis-dissolving, Danggui and Danshen were reported to ameliorate PF via diminishing fibroblast proliferation, inflammatory inhibition, and oxidation resistance.[21,22] Moreover, our previous work has demonstrated that QFHXD alleviates lipopolysaccharide-induced acute lung injury via regulating the TLR4/NF-κB pathway-mediated inflammation.[15] Taken together, as a prescription that incorporates the aforementioned CMHs, QFHXD appears to possess a promising anti-PF potential. However, studies specifically investigating the anti-PF activity of QFHXD are unavailable, much less its underlying functional mechanisms or effective constituents, prompting the present investigation into these very questions.

To investigate QFHXD's anti-PF action, a well-established bleomycin (BLM)-induced PF mouse model was employed in the present study.[23] Serum pharmacochemistry and lung tissue distribution were performed to track the potential bioactive components of QFHXD using ultra-high-performance liquid chromatography coupled with Q-Exactive quadrupole-orbitrap mass spectrometry (UPLC-Q-Orbitrap-MS/MS). Guided by an established compound-target-disease network and transcriptome sequencing data, bioinformatic analyses were carried out to decipher the key biological processes and signaling pathways underpinning the anti-PF efficacy of QFHXD, followed by experimental validation. Through in vitro experiments and molecular docking, anti-PF compounds targeting specific PF-related targets were identified. This study will lay the groundwork to support the clinical translation of QFHXD for PF treatment.

Materials and Methods

Drugs and Reagents

QFHXD freeze-dried powder was prepared by the Zhejiang Key Laboratory of Traditional Chinese Medicine for the Prevention and Treatment of Senile Chronic Diseases. All herbs used in QFHXD were provided by the TCM pharmacy of Hangzhou First People's Hospital. Loganin (T90594), phillyrin (B20725), baicalein (B20571), baicalin (B20570), wogonin (B20489), wogonoside (B20488), oroxylin A (T98415), peimine (B20080), peiminine (B20081), tanshinone IIA (B20257), nobiletin (B20199), paeoniflorin (B21148), albiflorin (B21149), and praeruptorin A (B20035) were purchased from Yuanye Biotechnology Co., Ltd. (Shanghai, China). All compounds had purities greater than 98%. BLM (99.03%, HY-17565), human TGF-β1 protein (HY-P7118), and SB-431542 (HY-10431) were obtained from MedChemExpress. Isoflurane (R510-22-10) was purchased from RWD Life Science Co., Ltd. (Shenzhen, China). Paraformaldehyde fixative (4%, E672002) was supplied by Sangon Biotechnology Co., Ltd. (Shanghai, China). Hematoxylin & Eosin (H&E) staining kit (C0105) and Hoechst 33342 (C1022) were purchased from Beyotime Biotechnology Co., Ltd. (Shanghai, China). Masson staining kit (G1006) and bovine serum albumin (BSA, GC305006) were bought from Servicebio Technology Co., Ltd. (Wuhan, China). Terminal Deoxynucleotidyl Transferase-mediated dUTP Nick-End Labeling (TUNEL) detection kit (HKI0010) and 3,3'-Diaminobenzidine Tetrahydrochloride (DAB) color development kit (HKI0039) were purchased from HaoKe Biotechnology Co., Ltd. (Hangzhou, China). RNA Isolator Total RNA Extraction Reagent (R401-01) and ChamQ Universal SYBR qPCR Master Mix (Q711) were purchased from Vazyme Biotechnology Co., Ltd. (Nanjing, China). ABScript III RT Master Mix for qPCR with gDNA Remover (RK20429) was purchased from ABclonal Biotechnology Co., Ltd. (Wuhan, China). Anti-α-SMA (ab7817), anti-MMP9 (ab283575), anti-Fibronectin (ab199056) for immunohistochemical staining, anti-Fibronectin (ab2413) for immunofluorescence, and anti-Collagen I (ab260043) antibodies were purchased from Abcam (Cambridge, United Kingdom). Anti-Caspase-3 antibody (#9662) was purchased from Cell Signaling Technology (Beverly, MA, United States). Mouse KL-6 (ZC-37730), TGF-β1 (ZC-39043), TLR2 (ZC-37839), TLR4 (ZC-37841), NF-κB (ZC-38232), TNF-α (ZC-39024), IL-1β (ZC-37974), IL-6 (ZC-37988), CCL2 (ZC-38588), SPP1 (ZC-57360), and ELISA kits were purchased from ZCi Biotechnology Co., Ltd. (Shanghai, China). Dimethyl sulfoxide (DMSO, 276855) was purchased from Sigma-Aldrich (Saint Louis, MO, United States). Dulbecco's Modified Eagle's

Medium (DMEM, 11965–092) was purchased from Gibco. Fetal bovine serum (FBS, 35–016-CV) was purchased from Corning. Cell Counting Kit-8 (CCK-8, BS350A) was purchased from Biosharp (Hefei, China).

Experimental Animals

Eighty-eight healthy adult male C57BL/6J mice (20–22 g) and twenty-four healthy adult male specific-pathogen-free-grade Sprague Dawley (SD) rats (245–255 g) were provided by Shanghai SLAC Laboratory Animal Co., Ltd. (Shanghai, China, Certificate No.: SCXK [Hu] 2022–0004). All animal studies were conducted in accordance with the guidance of the Care and Use of Laboratory Animals published by the US National Institutes of Health (NIH Publication No.85–23, revised 1996), and experimental protocols were approved by the Laboratory Animal Welfare and Ethics Committee of Zhejiang Center of Laboratory Animals (Approval number: ZJCLA-IACUC-20010760). The mice and rats were housed in an air-conditioned room (25 °C ± 1 °C, relative humidity of 45% ± 5%, 12-h light/dark cycle) with free access to clean water and food. While mice were employed for the pharmacodynamic evaluation of QFHXD against PF, rats were selected for serum pharmacochemistry due to their suitability for serial blood collection. Before the experiments, all animals were raised adaptively for one week.

Preparation of QFHXD Freeze-Dried Powder

According to the prescribed proportion, 9 g Jinyinhua, 15 g Lianqiao, 9 g Huangqin, 15 g Pugongying, 9 g Zhebeimu, 12 g Danggui, 12 g Danshen, 9 g Chenpi, 30 g Yiyiren, 15 g Baishao, 9 g Chaihu, 12 g Suoluoguo, 9 g Yujin, 9 g Xiangfu, 12 g Zisugeng, 9 g Qianhu, 9 g Kuxingren, and 9 g Jiegeng were mixed and soaked in 8 volumes of water for 30 min. The mixture was decocted thrice for 60 min each time. After filtration, the combined extracts were concentrated to 200 mL and freeze-dried under vacuum to generate QFHXD powder. The extraction yield was 14.8%.

Sample Preparation for Chemical Characterization of QFHXD in vitro

Freeze-dried QFHXD powder (100 mg) was dissolved in 1 mL ultrapure water, followed by ultrasound extraction for 60 min. After centrifugation at 14,000 rpm for 10 min, the supernatant was collected, diluted 5-fold with ultrapure water, and then analyzed by UPLC-Q-Orbitrap-MS/MS.

Sample Preparation for Chemical Profiling of Absorbable Components of QFHXD in vivo

After 12 h of fasting, twelve rats were randomly assigned to either a control group (n = 6) or a QFHXD group (n = 6). The QFHXD group received 6.62 g/kg (twice the clinical dose) of QFHXD by intragastric administration, while the control group received an equal volume of ultrapure water. The rats were anesthetized with isoflurane. The blood samples (0.5 mL) were respectively collected from the orbital venous plexuses at 0.25 h, 0.5 h, 0.75 h, 1 h, 1.5 h, 2 h, 3 h, 4 h, 6 h, 8 h, and 12 h following a single administration of QFHXD, and then transferred into heparinized tubes to isolate the plasma after centrifuging at 3500 rpm for 15 min at 4 °C. Equal amounts of plasma from different time points were merged for subsequent processing. For protein precipitation, 450 μL of methanol-acetonitrile (2:1, *v/v*) was added to 150 μL of pooled plasma. After vortex shaking, the mixture was ultrasonically extracted for 10 min in an ice-water bath and stored at −40 °C for 30 min. Following centrifugation (12,000 rpm, 10 min, 4 °C), 500 μL of supernatant was obtained and dried with nitrogen gas. The residue was redissolved with 150 μL of methanol-acetonitrile-water (2:1:1, *v/v/v*), followed by vortexing (1 min), ultrasound extraction (3 min), and stored at −40 °C overnight. After a final centrifugation step at 12,000 rpm for 10 min at 4 °C, the supernatant (100 μL) was transferred to a liquid glass-lined tube for UPLC-Q-Orbitrap-MS/MS analysis.

Sample Preparation for Study on Lung Tissue Distribution of Main Constituents in QFHXD

After fasting for 12 h, twelve rats were randomly divided into the control group (n = 6) and QFHXD group (n = 6). The rats in the QFHXD group received oral administration of QFHXD (6.62 g/kg), while the control group was given the

same volume of ultrapure water. At 2 h post-dosing, the rats were anesthetized with isoflurane and euthanized by cervical dislocation for lung tissue collection. The tissues were rinsed with pre-cooled normal saline and stored at −80 °C for subsequent processing. Each tissue sample (100 mg) was homogenized with 600 μL pre-cooled methanol-water (4:1, *v/v*) using a tissue homogenizer. The tissue homogenate was ultrasonically extracted for 10 min in an ice-water bath and stored at −40 °C overnight. After centrifuging at 12,000 rpm for 10 min at 4 °C, the supernatant (500 μL) was collected and dried with nitrogen gas. The residue was reconstituted in 300 μL of methanol-acetonitrile-water (2:1:1, v/v/v), vortexed for 30s, ultrasound extraction for 3 min, and then stored at −40 °C for 2 h. Following a final centrifugation, the supernatant (150 μL) was transferred to a liquid glass-lined tube for UPLC-Q-Orbitrap-MS/MS analysis.

Chromatographic and Mass Spectrometric Conditions

The chromatographic separation was conducted on a Waters ACQUITY UPLC I-Class Plus system using a HSS T3 column (100 mm × 2.1 mm, 1.8 μm) maintained at 45 °C. The mobile phase consisted of A (formic acid aqueous solution) and B (acetonitrile). The gradient elution program was carried out as follow: 0–2 min, 5%-5% B; 2–4 min, 5%-30% B; 4–8 min, 30%-50% B; 8–10 min, 50%-80% B; 10–14 min, 80%-100% B; 14–15 min, 100%-100% B; 15–15.1 min, 100%-5% B; 15.1–16 min, 5%-5% B. The flow rate was set at 0.35 mL/min, and the injection volume was 5 μL. Mass spectrometry (MS) analysis was performed using a Q-Exactive quadrupole-orbitrap mass spectrometer equipped with a heated-electrospray ionization (HESI) source (Thermo Fisher Scientific, Waltham, United States). Both positive electrospray ionization (ESI^+) and negative electrospray ionization (ESI^-) modes were employed to capture the mass spectrometric signals. The main MS parameters were set as follow: scan range, m/z 100–1500; spray voltage, 3800 V for ESI^+ and −3000 V for ESI^-; capillary temperature, 320 °C; auxiliary gas heater temperature, 350 °C; sheath gas flow rate, 35 Arb; auxiliary gas flow rate, 8 Arb; full MS resolution, 60,000; MS/MS resolution, 15,000.

MS Data Processing and Component Identification

The raw MS data were processed by Progenesis QI software (Version 3.0, Nonlinear, Dynamics, Newcastle, United Kingdom) for baseline filtering, peak identification, integral, retention time correction, peak alignment, and normalization. Compound identification was performed against the LuMet-TCM database of standard substances (OE Biotechnology Co., Ltd. Shanghai, China) by matching precise mass-to-charge ratio (m/z), fragment ions, isotopic distribution, and retention time (each assigned a score of 20). Compounds with a total score exceeding 50 were considered primary constituents of QFHXD in vitro. Among the identified compounds, those that demonstrated a statistically higher abundance (Fold Change>2 and P-value < 0.05) in the QFHXD group compared to the control group were defined as QFHXD's absorbable components in vivo or as constituents distributed to the lung. Fold Change = peak area of compound in QFHXD group/peak area of compound in control group.

BLM-Induced PF Model and Drug Intervention

Eighty-eight mice were randomly allocated to control (n = 16), BLM-induced PF model (n = 40), QFHXD low dose (QFHXD-L, 4.78 g/kg, n = 16), and QFHXD high dose (QFHXD-H, 9.56 g/kg, n = 16) groups. Based on our previous report,[15] QFHXD-L was converted from the clinical dosage using the following formula: QFHXD-L = 213 g × 14.8% × 9.1/60 kg (the clinical dosage for adult was 213 g/person/day, the extraction yield was 14.8%, the equivalent-dose ratio of human and mouse was 9.1, and the average weight of adult was 60 kg). The mice in QFHXD groups underwent a 5-day pretreatment with daily gavage. On day 6, 60 min after QFHXD administration, the PF model was initiated by a single intratracheal instillation of saline solution containing BLM (2.5 mg/kg),[23] while controls received an equal volume of normal saline. Daily QFHXD treatment resumed 24 h post-modeling and continued for 21 days. The control and model groups received ultrapure water (10 mL/kg) daily. The weight and survival were recorded throughout.

Histopathology

At 24 h after the last dose, the mice (n = 6 per group) were anesthetized with isoflurane and perfused. The lung tissues were then collected and fixed with 4% paraformaldehyde solution for 48 h. After dehydration and embedding, the paraffin-embedded tissues were cut into 3 μm-thick slices. H&E staining and Masson's trichrome staining of sections were performed according to the manufacturer's protocols. The images were acquired using an automatic digital slide scanning system (KF-PRO-120,

KFBIO, China) and observed with the accompanying software (KFBIO Digital Slide Viewer, Version 1.7.0.21). The severity of PF was semi-quantitatively evaluated using the Ashcroft score.[24] Eight observed fields in each section were scored, and the average score was calculated.

Collection of PF-Related and Bioactive Components-Relevant Targets

The online databases, including GeneCards (https://www.genecards.org/), DisGeNET (https://www.disgenet.org/), and Comparative Toxicogenomics Database (CTD, https://ctdbase.org/) were retrieved to acquire PF-relevant targets with the keyword "pulmonary fibrosis".[25,26] Targets with a Relevance Score > 8 in GeneCards and an Inference Score > 80 in CTD were selected. After identifying QFHXD's bioactive components in vivo, their potential targets were collected from the high-throughput experiment- and reference-guided database of traditional Chinese medicine (HERB) (https://herb.ac.cn/) and Traditional Chinese Medicine Systems Pharmacology Database and Analysis Platform (TCMSP) (https://old.tcmsp-e.com/tcmsp.php/).[27,28] For compounds that were not retrieved, the Swiss Target Prediction webserver (https://www.swisstargetprediction.ch/) and PubMed (https://www.ncbi.nlm.nih.gov/pubmed/) were employed to replenish compound-target information.[25] The targets with a Probability more than 0 in the Swiss Target Prediction web server were retained. The representative component-target network was visualized using R (Version 4.0.2, https://www.r-project.org/).

Network Construction and Detailed Analysis

To establish an integrated component-target-disease network, the overlapping targets between disease-target and component-target databases were determined using a Venn diagram,[26] and visualized with Cytoscape (Version 3.7.2). To further investigate the molecular mechanisms of QFHXD against PF, Gene Ontology (GO) and Kyoto Encyclopedia of Genes and Genomes (KEGG) enrichment analyses were performed with the Database for Annotation, Visualization and Integration Discovery (DAVID, https://david.ncifcrf.gov/).[25,26] The results of GO and KEGG were visualized with ImageGP (https://www.bic.ac.cn/ImageGP/).[29] The protein-protein interaction (PPI) network of overlapping targets was generated using the Search Tool for Recurring Instances of Neighboring Genes (STRING) database (Version 12.0, https://string-db.org/). Using the Molecular Complex Detection (MCODE) plugin in Cytoscape, the most significant cluster of the PPI network was selected based on its MCODE score and node numbers.[30] The subnetwork was presented in Degree order. The cytoHubba plugin was utilized to rank the nodes of the PPI network based on the maximal clique centrality (MCC) algorithm.[31] The associations between identified key targets and important signaling pathways were visualized using Cytoscape.

Ribonucleic Acid Sequencing (RNA-Seq) and Bioinformatics Analysis

At 24 h after the final administration, lung tissues were harvested from mice in the BLM-induced PF model and QFHXD-H groups. According to the manufacturer's instructions, the libraries were constructed using the VAHTS Universal V6 RNA-Seq Library Prep Kit (Vazyme, China) following the extraction and assessment of total RNA samples. The transcriptome sequencing was performed with an Illumina Novaseq 6000 platform, and then the clean reads of each sample were obtained by removing low-quality reads. The clean reads were mapped to the reference genome using the HISAT2 program (https://daehwankimlab.github.io/hisat2/). Fragments Per Kilobase of exon model per Million mapped fragments (FPKM) of each gene was calculated, and the read counts of each gene were acquired by HTSeq-count (https://htseq.readthedocs.io/en/master/). The DESeq2 (https://bioconductor.org/packages/release/bioc/html/DESeq2.html) was applied for differential expression analysis.[32] The differentially expressed genes (DEGs) were confirmed based on the threshold of Q-value < 0.05 and |log2FoldChange| ≥1. The volcano plot and clustering heat map of DEGs were produced by an online platform for data analysis and visualization (https://www.bioinformatics.com.cn). By comparing with overlapping targets from network pharmacology, the selected DEGs were imported into DAVID for KEGG enrichment analysis. Using the STRING database and Cytoscape, the pivotal DEGs within significant pathways were identified based on Degree and MCC topological algorithms.

TUNEL Assay

The anti-apoptotic effect of QFHXD was evaluated by TUNEL detection. Briefly, the sections were incubated with TUNEL working solution for 60 min at 37 °C following dewaxing, rehydration, and permeabilization. After nuclear counterstaining, the slides were scanned using a Panoramic MIDI automatic digital slide scanner (3DHISTECH Ltd., Budapest, Hungary). TUNEL-positive apoptotic cells were counted in five randomly selected fields per section using the SlideViewer software (Version 2.5.0.143918).

Immunohistochemical Staining

Immunohistochemical staining was performed in accordance with standard procedures. Briefly, the paraffin-embedded sections were dewaxed, rehydrated, and subjected to antigen retrieval. After blocking endogenous peroxidase activity and non-specific sites, the slices were subsequently treated overnight with the primary antibodies of anti-α-SMA (1:500), anti-Fibronectin (1:1000), anti-MMP9 (1:500), and anti-Caspase-3 (1:1000) at 4 °C. After incubation with the corresponding secondary antibodies, the sections were colored with DAB and counterstained with hematoxylin. The automatic digital slide scanning system (KF-PRO-120, KFBIO, China) was exploited to gather the images. For each sample, eight random regions were selected using the KFBIO digital slide viewer (Version 1.7.0.21), and protein expression was quantified with ImagePro Plus software (Version 6.0).

Enzyme-Linked Immunosorbent Assay (ELISA)

At 24 h post-final dose, blood samples (n = 8 per group) were intravenously taken from mice under isoflurane anesthesia. The serum was isolated by centrifugation (3500 rpm, 15 min, 4 °C). The mice were then euthanized by cervical dislocation and lung tissues (n = 6 per group) were rapidly harvested. After weighing, homogenization, and centrifugation (10,000 rpm, 10 min, 4 °C), the tissue supernatants were obtained. The protein contents of Krebs von den Lungen-6 (KL-6), transforming growth factor-beta1 (TGF-β1), and chemokine (C-C motif) ligand 2 (CCL2) in serum samples as well as the protein levels of toll-like receptor 2 (TLR2), toll-like receptor 4 (TLR4), nuclear factor-kappa B (NF-κB), tumor necrosis factor-alpha (TNF-α), interleukin-1 beta (IL-1β), interleukin-6 (IL-6), secreted phosphoprotein 1 (SPP1), CCL2, and TGF-β1 in lung supernatants were detected and calculated using the ELISA method in line with manufacturer's instructions.

Real-Time Quantitative Polymerase Chain Reaction (RT-qPCR) Analysis

The total RNA samples were extracted from lung tissues (n = 5 per group). To measure the transcriptional levels of validated genes, RT-qPCR reactions were carried out with the universal SYBR premix using the Applied Biosystems QuantStudio 6 Flex Real-Time PCR system (Version 1.7.2, Thermo Fisher Scientific, Waltham, United States). Glyceraldehyde-3-phosphate dehydrogenase (GAPDH) was selected as the internal control gene, and the relative mRNA expression levels of validated genes were quantified using the $2^{-\Delta\Delta CT}$ method. The primer sequences were presented in Supplementary Table S1 and synthesized by SUNYA Biotechnology Co., Ltd. (Hangzhou, China).

Cell Culture and Treatment

Human embryonic lung fibroblast line (MRC-5 cells) was obtained from the Cell Bank of the Chinese Academy of Sciences (Shanghai, China). The cells at a density of 4×10^3 cells/well were cultured in DMEM supplemented with 10% FBS and 1% penicillin-streptomycin at 37 °C under a humidified atmosphere with 5% CO_2. Upon reaching 70% confluence, the cells were serum-starved for 24 h. Then, the cells were treated with either TGF-β1 (20 ng/mL), TGF-β1 (20 ng/mL) plus SB-431542 (2 μM), TGF-β1 (20 ng/mL) plus QFHXD (100 μg/mL and 200 μg/mL), or TGF-β1 (20 ng/mL) plus each component (1 μM). The concentrations of QFHXD and its 14 compounds were determined based on prior cytotoxicity assays (Supplementary Figure S1). The control cells were incubated with 0.1% dimethyl sulfoxide (DMSO) solvent. After 48 h of incubation, the cells were harvested for subsequent experiments.

Cell Immunofluorescence

Following 48 h of TGF-β1 stimulation, the collected cells were fixed with 4% paraformaldehyde solution for 30 min. After permeabilization and blocking, an overnight incubation with anti-Fibronectin (1:200) and anti-Collagen I (1:200) antibodies was performed at 4 °C, followed by staining with the corresponding secondary antibodies. The nuclei were counterstained with Hoechst (1:1000) for 10 min at 37 °C. The fluorescence images were acquired using a Micro Confocal High-Content Imaging System (ImageXpress, Molecular Devices, United States) and analyzed with the MetaXpress PowerCore Software (Version 1.5.0.17).

Molecular Docking

The files of X-ray crystal structures of target proteins were downloaded from the Protein Data Bank (PDB) database (https://www.rcsb.org/pdb/). The structure files (SDF format) of active constituents were downloaded from the PubChem (https://pubchem.ncbi.nlm.nih.gov/) database, and then converted into three-dimensional structures (MOL2 format) using the OpenBabel software (Version 2.3.2). Both receptor and ligand files were subsequently processed with the AutoDock software (Version 4.2.6) to generate PDBQT files. Molecular docking simulations were performed using the AutoDock Vina software (Version 1.2.0) to evaluate binding affinity. A grid box was centered on the receptor protein and adjusted to encompass the predicted binding pocket. The receptor-ligand interaction complexes were visualized with the PyMOL software (Version 2.5).

Statistical Analysis

The experimental data were analyzed using SPSS software (Version 21.0, IBM Corp., United States).The Shapiro–Wilk test and Levene's test were used to assess the normality and homogeneity of variance of quantitative data, respectively. A two-tailed Student's *t*-test was used to compare the two groups, as the data were normally distributed. When the data from multiple groups met the assumptions of normality and homogeneity of variance, a one-way analysis of variance (ANOVA) with Dunnett's post-hoc test was applied. If these assumptions were violated, the Kruskal–Wallis test was employed, followed by Dunn's post-hoc test for pairwise comparisons. The data were presented as mean ± SD, except for RT-qPCR data of inflammatory genes, which were expressed as mean ± SEM. Survival curves were compared using the Log rank test. A value of $P < 0.05$ was considered statistically significant. The GraphPad Prism software (Version 8.0.2) was employed for graphing.

Results

QFHXD Intervention Improved Survival and Alleviated Fibrotic Phenotypes in BLM-Induced PF Mice

As illustrated in the experimental design (Supplementary Figure S2), mouse weight and survival were monitored daily following BLM stimulation. Compared with the healthy mice, BLM-stimulated PF mice exhibited apparent weight loss and reduced survival within the experimental period (Figure 1A and B). As expected, QFHXD intervention observably enhanced body weight and rescued survival, and lowered mortality from 55% to 12.5% (Figure 1A and B). Histopathological evaluation via H&E and Masson staining revealed that BLM exposure severely caused lung lesions, including damage to alveolar architecture, fibrous thickening of alveolar walls, collapse of alveolar spaces, numerous aggregation of inflammatory cells, proliferation of fibrous tissues, formation of fibrous masses, and abundant collagen deposition (Figure 1C). These pathological changes were reflected by a markedly elevated Ashcroft score (Figure 1D). In contrast, administration of QFHXD at different doses significantly mitigated BLM-induced fibrotic lesions and decreased Ashcroft grade of PF (Figure 1C and D). Consistent with these findings, immunohistochemical staining demonstrated that the abnormally elevated expression of pro-fibrotic markers alpha-smooth muscle actin (α-SMA) and Fibronectin (FN) in PF mice was significantly suppressed by QFHXD treatment (Figure 1C, E and F). Similarly, QFHXD markedly reversed the aberrantly upregulated transcriptional levels of pro-fibrotic genes (Fn1 and Col1a1) in lung samples of PF mice (Figure 1G and H). In addition, ELISA results showed that QFHXD intervention decreased the unconventionally

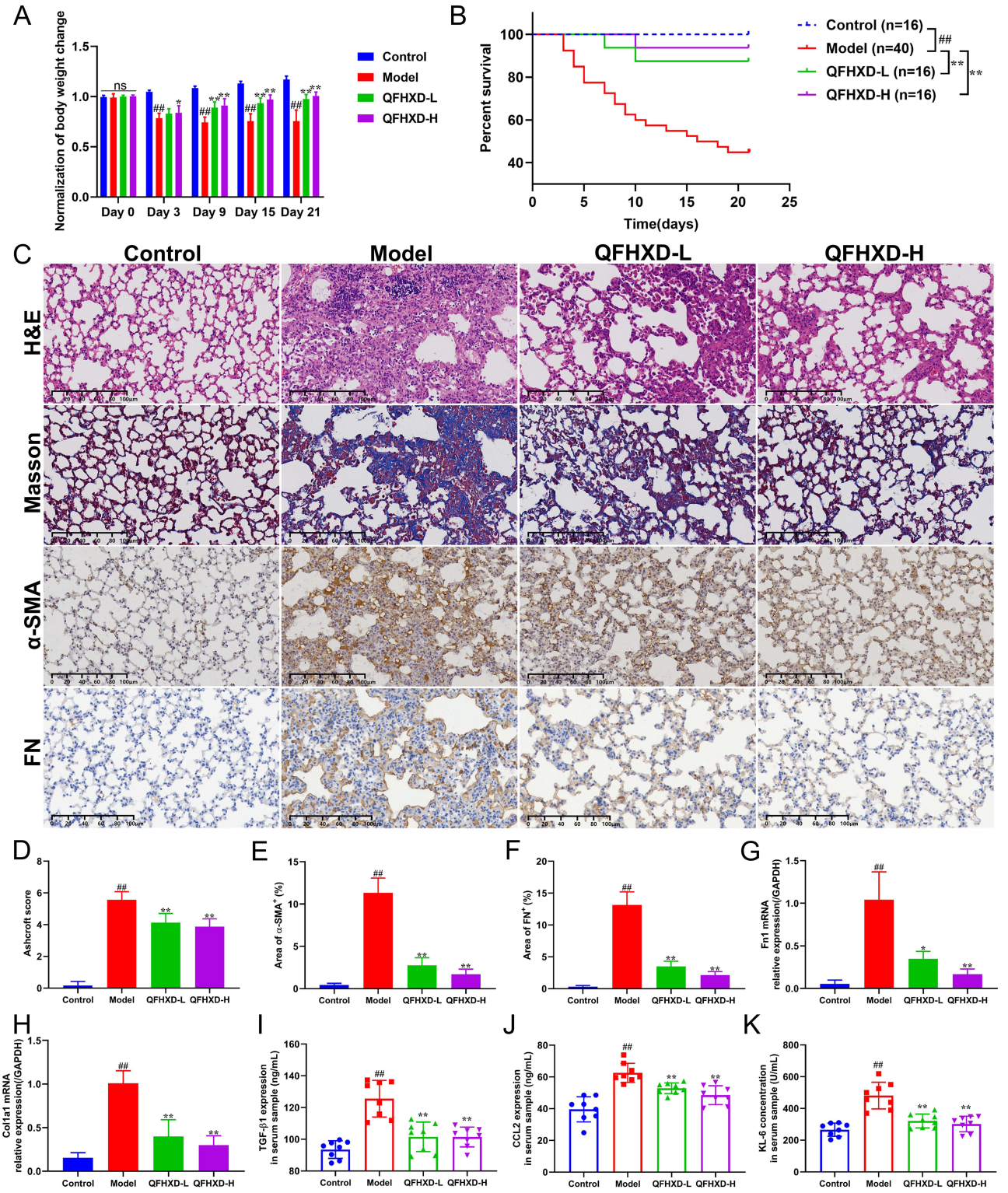

Figure 1 Effects of QFHXD on histopathology and pro-fibrotic markers in BLM-induced PF mice. (**A**) Dynamic changes in body weight. (**B**) The Kaplan-Meier survival curve of each group. Compared with the model group, Treatment with different doses of QFHXD markedly boosted the survival rate of PF mice. (**C**) The representative images of lung sections stained with H&E, Masson's trichrome, and immunohistochemical staining for α-SMA and FN proteins (×200 magnification, scale bar: 100 μm, n = 6). (**D**) Ashcroft score for grading PF severity (n = 6). Quantification of immunohistochemical results of α-SMA (**E**) and FN (**F**) expression (n = 6). The relative mRNA levels of Fn1 (**G**) and Col1a1 (**H**) in lung samples of each group (n = 5). QFHXD administration effectively mitigated fibrotic lesions, inhibited collagen deposition, and decreased the expression of pro-fibrotic markers. Serum levels of TGF-β1 (**I**), CCL2 (**J**), and KL-6 (**K**) were measured by ELISA (n = 8). Data are displayed as the mean ± SD. $^{\#\#}P < 0.01$ versus the control group; $^{*}P < 0.05$, and $^{**}P < 0.01$ versus the model group. Model, BLM-induced PF model; QFHXD-L, QFHXD low dose (4.78 g/kg); QFHXD-H, QFHXD high dose (9.56 g/kg).

https://doi.org/10.2147/DDDT.S592770

increased serum levels of pro-fibrotic and inflammatory mediators TGF-β1 and CCL2, as well as alveolar epithelial injury marker KL-6 (Figure 1I–K).

Identification of Potential Bioactive Components of QFHXD in vivo

To identify the potential bioactive substances for further elucidating anti-PF functional mechanisms and discovering pharmacodynamic constituents of QFHXD, serum pharmacochemistry and lung tissue distribution analyses were conducted using UPLC-Q-Orbitrap-MS/MS. The base peak chromatograms in both ESI^+ and ESI^- modes were respectively acquired for in vitro and in vivo samples using the developed gradient program within 16 min (Figure 2). A total of 37 prototype components from QFHXD were characterized as the absorbable constituents in the QFHXD-containing plasma (Figure 2A and B). The main parameters and sources of these absorbable compositions were summarized in Table 1. A total of 24 prototype constituents from QFHXD were identified in lung tissues following QFHXD administration (Figure 2C and D). Table 2 displayed the primary parameters and sources of these lung-distributed compounds. Notably, 15 prototype components, including neoamygdalin, loganin, paeoniflorin, peiminine, wogonin, oroxylin A, and neocryptotanshinone, were simultaneously detected in both the bloodstream and lung tissues. Broadly speaking, the absorbable

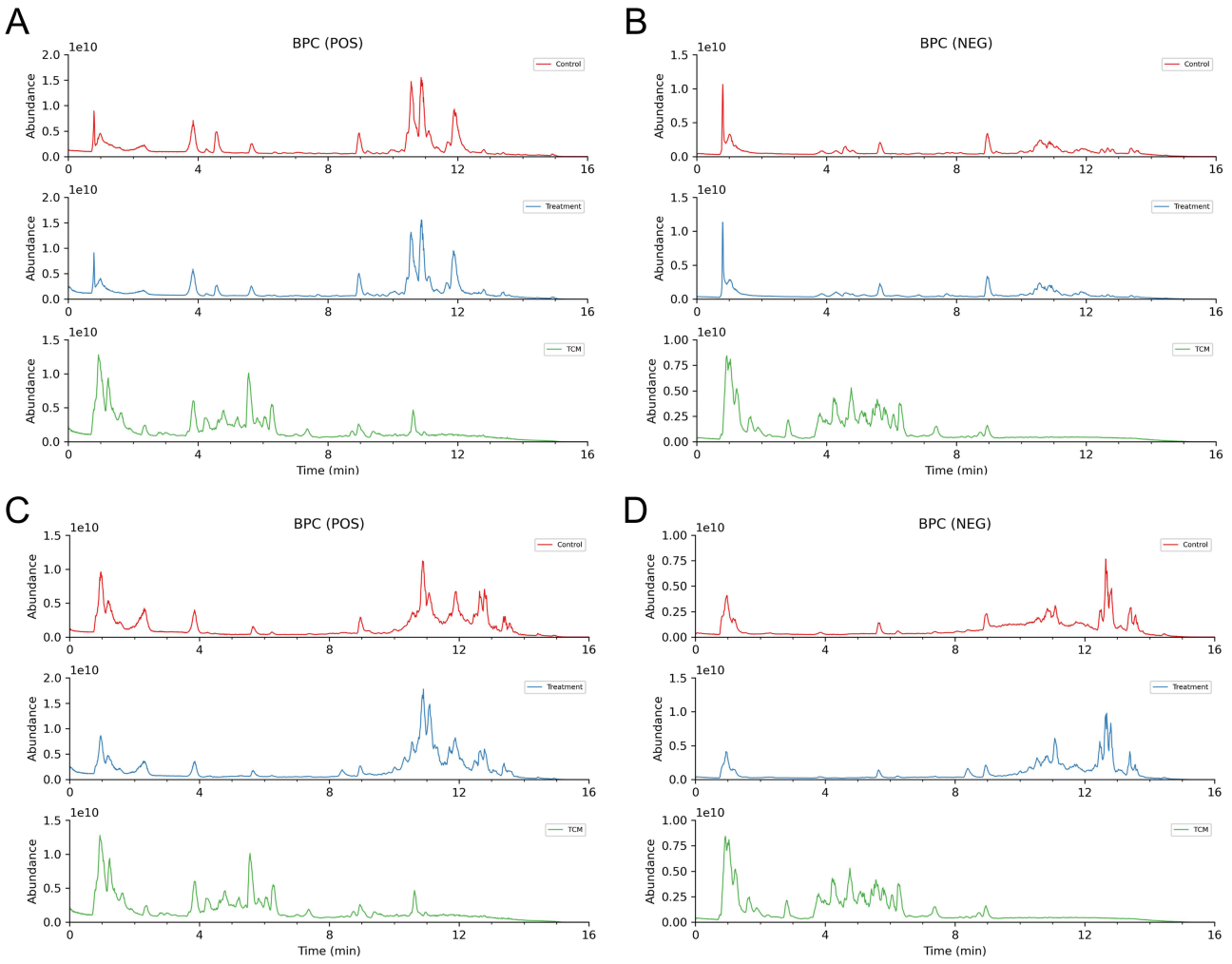

Figure 2 Chemical profiling of QFHXD in rat plasma and lung tissue by UPLC-Q-Orbitrap-MS/MS. The representative base peak chromatograms of QFHXD acquired in both positive (**A**) and negative (**B**) ion modes for serum pharmacochemistry (Control, blank plasma; Treatment, QFHXD-containing plasma; TCM, QFHXD sample in vitro). The typical base peak chromatograms of QFHXD obtained in both positive (**C**) and negative (**D**) ion modes for lung tissue distribution (Control, blank lung tissues; Treatment, QFHXD-containing lung tissues; TCM, QFHXD sample in vitro).
Abbreviations: BPC, base peak chromatogram; POS, positive ion mode; NEG, negative ion mode.

https://doi.org/10.2147/DDDT.S592770

Table 1 Identification of Absorbable Components of QFHXD in Rat Plasma by UPLC-Q-Orbitrap-MS/MS

NO.	RT (Min)	Formula	Adducts	Theoretical m/z	Detected m/z	Mass Error (ppm)	Identification	Source
1	3.91	$C_{14}H_{20}O_7$	[M-H]-, [M+FA-H]-	345.1193	345.1177	−4.79	Salidroside	HQ, LQ
2	4.11	$C_{16}H_{22}O_{11}$	$[M+NH_4]+$, [M+Na]+	413.1055	413.1038	−4.06	Secologanoside	JYH
3	4.12	$C_{17}H_{26}O_{11}$	[M+FA-H]-	451.1459	451.1442	−3.82	Shanzhiside methyl ester	DS
4	4.22	$C_{16}H_{22}O_{10}$	[M-H]-, [M+FA-H]-, [2M-H]-	373.1140	373.1124	−4.23	Secologanic acid	JYH
5	4.24	$C_8H_8O_3$	[M-H]-	151.0401	151.0395	−3.70	4-Hydroxyphenylacetic acid	LQ
6	4.30	$C_{20}H_{27}NO_{11}$	[M+FA-H]-, [2M-H]-, [M-H]-	502.1568	502.1549	−3.74	Neoamygdalin	KXR
7	4.42	$C_{17}H_{26}O_{10}$	[M+FA-H]-	435.1510	435.1492	−4.10	Loganin	JYH
8	4.60	$C_{17}H_{24}O_{11}$	[M-H]-, [2M-H]-, [M+FA-H]-	403.1246	403.1230	−3.80	Secoxyloganin	JYH
9	4.62	$C_{23}H_{28}O_{11}$	[M+H]+	481.1704	481.1687	−3.70	Albiflorin	BS
10	4.68	$C_{14}H_{17}NO_6$	[M+FA-H]-	340.1040	340.1024	−4.76	Prunasin	KXR
11	4.68	$C_{17}H_{20}O_9$	[M-H]-	367.1035	367.1017	−4.73	3-O-Feruloylquinic acid	DG
12	4.70	$C_{23}H_{28}O_{11}$	[M-H]-, [2M-H]-, [M+FA-H]-	525.1615	525.1595	−3.98	Paeoniflorin	BS
13	4.84	$C_{26}H_{28}O_{13}$	[M+H]+	549.1603	549.1584	−3.49	Chrysin 6-C-glucoside 8-C-arabinoside	HQ
14	4.92	$C_{21}H_{18}O_{12}$	[M+H]+, [M+Na]+	463.0871	463.0852	−4.07	Luteolin 7-O-glucuronide	JYH
15	4.94	$C_{21}H_{20}O_{12}$	[M-H]-	463.0882	463.0869	−2.81	Isoquercitrin	JYH, CH
16	5.25	$C_{27}H_{45}NO_3$	$[M+H-H_2O]+$, [M+H]+	432.3472	432.3455	−4.00	Peimine	ZBM
17	5.29	$C_{27}H_{22}O_{12}$	[M-H]-, [2M-H]-	537.1038	537.1018	−3.87	Lithospermic acid	DS
18	5.41	$C_{27}H_{43}NO_3$	$[M+H-H_2O]+$, [M+H]+	430.3316	430.3298	−4.21	Peiminine	ZBM
19	5.41	$C_{20}H_{28}O_8$	[M+FA-H]-	441.1768	441.1749	−4.33	Lobetyolin	JG
20	5.56	$C_{21}H_{18}O_{11}$	[M-H]-	445.0776	445.0759	−3.85	Baicalin	HQ
21	5.69	$C_7H_6O_3$	[M-H]-	137.0244	137.0238	−4.12	Salicylic acid	XF, YJ, BS
22	5.79	$C_{27}H_{34}O_{11}$	[M+FA-H]-	579.2085	579.2064	−3.54	Phillyrin	LQ
23	5.83	$C_{27}H_{45}NO_3$	[M+H]+	432.3472	432.3455	−3.97	Isoverticine	ZBM
24	5.86	$C_{21}H_{18}O_{11}$	[M-H]-	445.0776	445.0761	−3.48	Glychionide A	HQ
25	6.05	$C_{22}H_{20}O_{11}$	[M+H]+, [M+K]+, [M+Na]+	461.1078	461.1060	−4.07	Oroxyloside	HQ
26	6.09	$C_{21}H_{18}O_{10}$	[M+H]+	431.0973	431.0955	−4.01	Chrysin-7-O-glucuronide	HQ
27	6.29	$C_{22}H_{20}O_{11}$	[M-H]-, [2M-H]-	919.1938	919.1921	−1.91	Wogonoside	HQ
28	7.37	$C_{15}H_{10}O_5$	[M-H]-	269.0455	269.0445	−3.76	Baicalein	HQ
29	7.82	$C_{12}H_{14}O_3$	[M-H]-	205.0870	205.0863	−3.30	2-Pentanoylbenzoic Acid	DG
30	8.71	$C_{55}H_{86}O_{24}$	[M-H]-	1129.5436	1129.5403	−2.91	Isoescin IB	SLZ
31	8.71	$C_{55}H_{86}O_{24}$	[M+H]+, $[M+NH_4]+$, [M+K]+, [M+Na]+	1131.5582	1131.5539	−3.83	Isoescin IA	SLZ
32	8.75	$C_{16}H_{12}O_5$	[M-H]-	283.0612	283.0601	−3.69	Wogonin	HQ
33	9.09	$C_{16}H_{12}O_5$	[M+H]+	285.0758	285.0747	−3.87	Oroxylin A	HQ
34	9.37	$C_{22}H_{24}O_9$	[M+H]+, [M+Na]+, [M+K]+	433.1493	433.1476	−3.95	3,5,6,7,8,3',4'-Heptamethoxyflavone	CP
35	9.65	$C_{18}H_{16}O_4$	[M-H]-	295.0976	295.0964	−4.01	Tanshinone VI	DS
36	9.83	$C_{18}H_{18}O_4$	[M+H]+	299.1278	299.1266	−4.12	Phenethyl ferulate	DG
37	10.47	$C_{19}H_{22}O_4$	[M-H]-	313.1445	313.1434	−3.58	Neocryptotanshinone	DS

Abbreviations: RT, Retention time; JYH, Jinyinhua; LQ, Lianqiao; HQ, Huangqin; PGY, Pugongying; ZBM, Zhebeimu; DG, Danggui; DS, Danshen; CP, Chenpi; YYR, Yiyiren; BS, Baishao; CH, Chaihu; SLG, Suoluoguo; YJ, Yujin; XF, Xiangfu; ZSG, Zisugeng; QH, Qianhu; KXR, Kuxingren; JG, Jiegeng.

and lung-distributed components identified in vivo represented the potential bioactive substances of QFHXD and were subjected to subsequent investigations.

Network Pharmacology Exploration of the Potential Key Anti-PF Targets and Mechanisms of QFHXD

Network pharmacology was employed to reveal the underlying regulatory mechanisms of QFHXD against PF. A disease-target dataset was constructed using 1830 PF-associated targets collected from multiple public databases (Figure 3A). Leveraging QFHXD's 46 potential bioactive ingredients identified in vivo (Tables 1 and 2), a compound-target dataset encompassing 525 related targets was established. Figure 3B exhibited the relevance network between 46 bioactive constituents and their top 50 related targets. Integrating the two datasets resulted in 323 overlapping targets (Supplementary Tables S2 and S3) as shown in a component-target-disease network (Figure 3C and D). The subsequent enrichment analyses revealed that these overlapping targets were significantly associated with inflammatory processes (inflammatory response,

https://doi.org/10.2147/DDDT.S592770

Table 2 Identification of Lung-Distributed Constituents of QFHXD in Rat by UPLC-Q-Orbitrap-MS/MS

NO.	RT (Min)	Formula	Adducts	Theoretical m/z	Detected m/z	Mass Error (ppm)	Identification	Source
1	4.31	$C_{20}H_{27}NO_{11}$	[M+FA-H]-, [2M-H]-, [M-H]-	502.1568	502.1547	−4.10	Neoamygdalin	KXR
2	4.42	$C_{17}H_{26}O_{10}$	[M+FA-H]-	435.1510	435.1491	−4.40	Loganin	JYH
3	4.60	$C_{17}H_{24}O_{11}$	[M-H]-, [2M-H]-, [M+FA-H]-	403.1246	403.1230	−3.96	Secoxyloganin	JYH
4	4.68	$C_{17}H_{20}O_9$	[M-H]-	367.1035	367.1016	−4.97	3-O-Feruloylquinic acid	DG
5	4.72	$C_{23}H_{28}O_{11}$	[M+FA-H]-, [2M-H]-, [M-H]-	525.1616	525.1594	−4.18	Paeoniflorin	BS
6	4.85	$C_{26}H_{28}O_{13}$	[M+H]+	549.1603	549.1583	−3.53	Chrysin 6-C-glucoside 8-C-arabinoside	HQ
7	5.14	$C_{27}H_{41}NO_3$	[M+H]+	428.3159	428.3141	−4.22	Peimisine	ZBM
8	5.40	$C_{27}H_{43}NO_3$	[M+H-H_2O]+, [M+H]+	430.3316	430.3298	−4.23	Peiminine	ZBM
9	5.79	$C_{21}H_{20}O_{11}$	[M-H]-	447.0933	447.0918	−3.34	Dihydrobaicalin	HQ
10	5.84	$C_{27}H_{45}NO_3$	[M+H]+	432.3472	432.3454	−4.20	Isoverticine	ZBM
11	5.87	$C_{21}H_{18}O_{11}$	[M-H]-	445.0776	445.0759	−3.87	Glychionide A	HQ
12	6.06	$C_{22}H_{20}O_{11}$	[M+H]+, [M+Na]+	461.1078	461.1059	−4.20	Oroxyloside	HQ
13	6.09	$C_{21}H_{18}O_{10}$	[M-H]-	429.0827	429.0809	−4.29	Chrysin-7-O-glucuronide	HQ
14	8.76	$C_{16}H_{12}O_5$	[M-H]-	283.0612	283.0600	−4.07	Wogonin	HQ
15	8.95	$C_{21}H_{22}O_8$	[M+Na]+, [M+K]+, [M+H]+	403.1387	403.1368	−4.83	Nobiletin	CP
16	9.09	$C_{16}H_{12}O_5$	[M+H]+	285.0758	285.0746	−4.01	Oroxylin A	HQ
17	9.38	$C_{22}H_{24}O_9$	[M+H]+, [M+K]+, [M+Na]+	433.1493	433.1476	−4.02	3,5,6,7,8,3',4'-Heptamethoxyflavone	CP
18	9.97	$C_{12}H_{14}O_2$	[M+H]+	191.1067	191.1060	−3.33	Butylphthalide	DG
19	10.01	$C_{12}H_{18}O_2$	[M+H]+	195.1380	195.1374	−2.84	Cnidilide	DG
20	10.20	$C_{12}H_{14}O_2$	[M+H-H_2O]+, [M+H]+	191.1067	191.1060	−3.49	Ligustilide	DG
21	10.47	$C_{19}H_{22}O_4$	[M-H]-	313.1445	313.1434	−3.73	Neocryptotanshinone	DS
22	10.63	$C_{21}H_{22}O_7$	[M+NH_4]+, [M+K]+, [M+Na]+, [M+H]+	404.1704	404.1689	−3.77	Praeruptorin A	QH
23	11.65	$C_{19}H_{18}O_3$	[M+Na]+, [M+K]+, [M+H]+	317.1149	317.1134	−4.64	Tanshinone IIA	DS
24	11.77	$C_{24}H_{28}O_7$	[M+NH_4]+, [M+K]+, [M+Na]+	446.2174	446.2159	−3.45	Praeruptorin E	QH

Abbreviations: RT, Retention time; JYH, Jinyinhua; LQ, Lianqiao; HQ, Huangqin; PGY, Pugongying; ZBM, Zhebeimu; DG, Danggui; DS, Danshen; CP, Chenpi; YYR, Yiyiren; BS, Baishao; CH, Chaihu; SLG, Suoluoguo; YJ, Yujin; XF, Xiangfu; ZSG, Zisugeng; QH, Qianhu; KXR, Kuxingren; JG, Jiegeng.

cellular response to tumor necrosis factor, and positive regulation of interleukin-8 production) and inflammatory signaling pathways (TNF signaling pathway, Toll-like receptor signaling pathway, and IL-17 signaling pathway) (Figure 4A and B). Meanwhile, the top 20 enriched biological processes and signaling pathways, such as apoptotic process, PI3K-Akt signaling pathway, and Apoptosis signaling pathway, were closely linked to apoptosis (Figure 4A and B). To further determine pivotal targets modulated by QFHXD, a PPI network of 323 overlapping targets was analyzed using MCODE plugin, revealing a key cluster of 119 nodes (ranked by Degree) and 5165 edges (Figure 4C). In addition, MCC algorithm in cytoHubba plugin ranked the top 15 targets (Figure 4D). Through integrating top 20 targets from component-target network (Supplementary Table S4), top 15 nodes based on Degree algorithm (Supplementary Table S5), top 15 targets based on MCC algorithm (Supplementary Table S5), 28 hub targets were prioritized. Linking these targets to focused pathways highlighted crucial candidates, such as TGFB1, MMP9, TLR4, RELA, NFKB1, IL6, IL1B, TNF, CASP3, BAX, and BCL2, involved in inflammatory and apoptotic mechanisms underlying QFHXD's anti-PF activity (Figure 4E), warranting follow-up experimental validation.

RNA-Seq Analysis Further Deciphered the DEGs and Anti-PF Mechanisms of QFHXD Intervention

Transcriptome sequencing was performed to compare fibrotic lung tissues from PF model mice with and without QFHXD treatment. At a threshold of Q-value < 0.05 and |log2FoldChange| ≥1, 2105 DEGs were identified in the QFHXD-H group versus the model group. Among these, 991 DEGs were upregulated and 1114 DEGs were downregulated, as visualized in the volcano plot (Figure 5A). The representative DEGs details were represented by a clustering heat map (Figure 5B). Compared 2105 RNA-seq-derived DEGs with 323 overlapping targets from established component-target-disease network pinpointed 63 common genes (Supplementary Table S6), that may represent the core anti-PF targets of QFHXD. KEGG enrichment analysis of 63 DEGs confirmed significant enrichment in inflammatory and apoptotic pathways, including PI3K-Akt signaling pathway, IL-17 signaling pathway, Toll-like receptor signaling pathway, and TNF signaling pathway (Figure 5C), underscoring their roles in

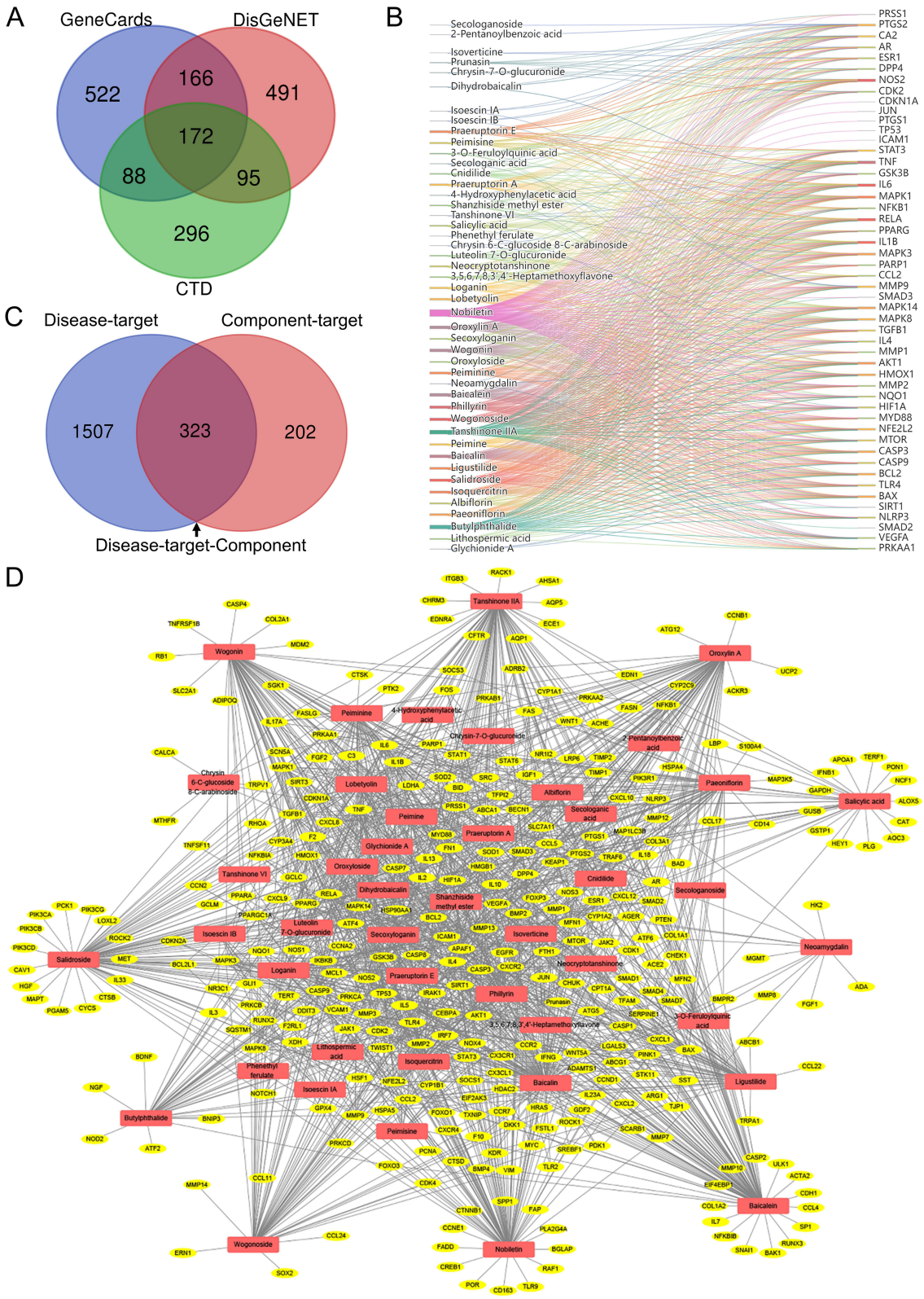

Figure 3 QFHXD component-target network and its relevance to PF-related targets. (**A**) Venn diagram of PF-associated targets obtained from several online databases. (**B**) A compound-target network of QFHXD. The network depicts 46 potential bioactive compounds and their top 50 regulated targets. (**C**) Venn diagram of merging disease-target and component-target datasets. The 323 overlapping targets represent potential candidates through which QFHXD may exert its multi-target therapeutic action in PF. (**D**) A component-target-disease network was visualized with Cytoscape. This network maps the associations between 323 PF-related targets (yellow color) and 46 potential bioactive ingredients of QFHXD (red color).

https://doi.org/10.2147/DDDT.S592770

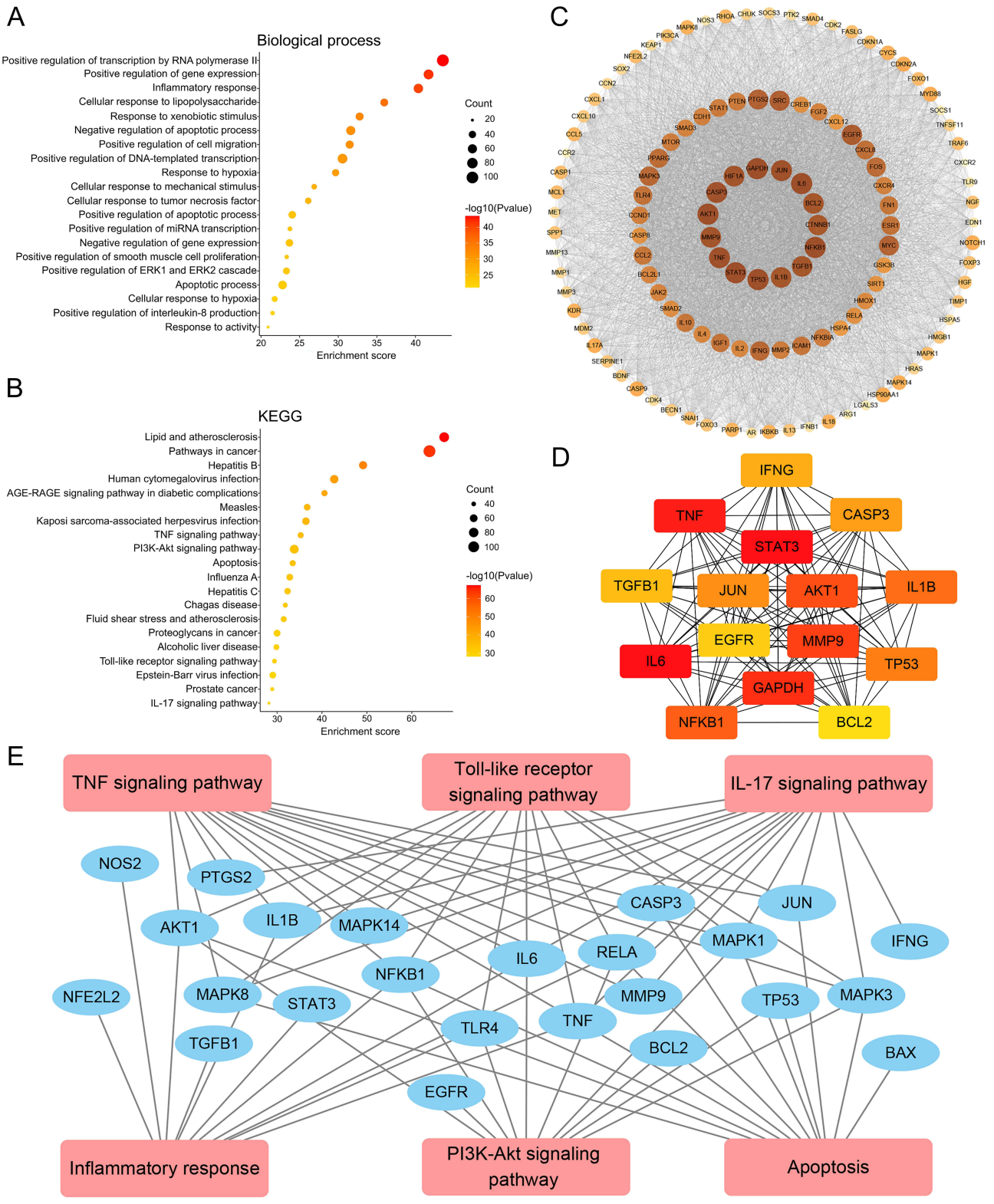

Figure 4 Enrichment analyses and identification of core anti-PF targets of QFHXD. (**A**) Top 20 enriched GO terms of biological processes. (**B**) Top 20 enriched KEGG signaling pathways. The results of enrichment analyses suggested that the beneficial effects of QFHXD on improving BLM-induced fibrotic phenotypes might be attributed to the regulation of inflammation and apoptosis. (**C**) MCODE module analysis of the PPI network. According to the MCODE score and node numbers, the most stable cluster was extracted from the PPI network. The node with a higher Degree value was expressed by the deeper color and larger size. (**D**) The top 15 targets of the PPI network were ranked based on MCC method. The node with the better centrality in the PPI network was expressed by the deeper color. (**E**) A correlation network linking identified hub targets to inflammatory and apoptotic mechanisms.

https://doi.org/10.2147/DDDT.S592770

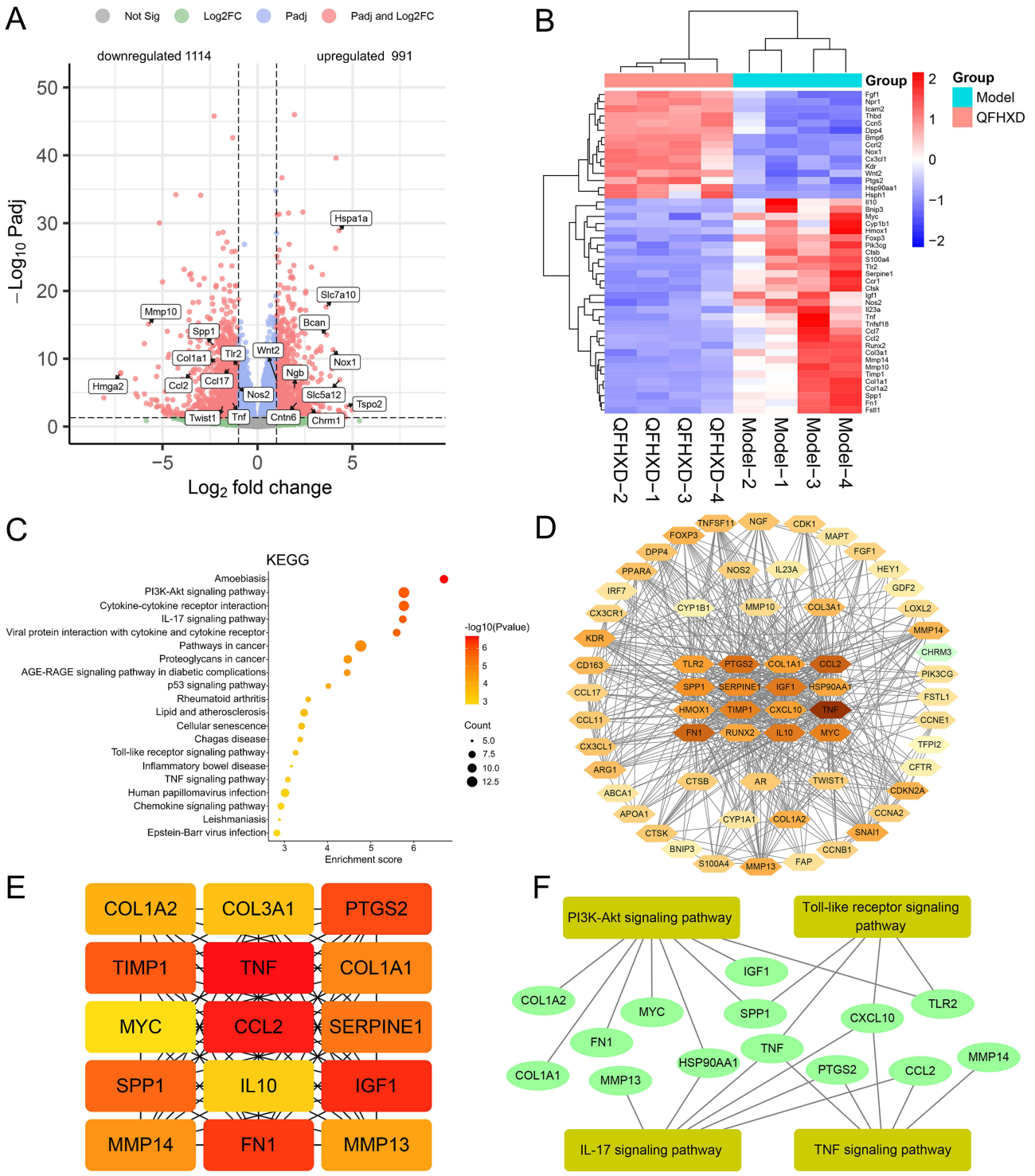

Figure 5 RNA-Seq analysis and identification of key DEGs. (**A**) Volcano plot of identified 2105 DEGs. Compared with the model group, 991 upregulated DEGs and 1114 downregulated DEGs were detected in the QFHXD-H group. (**B**) A clustering heat map of representative DEGs. Red color represented upregulation and blue color represented downregulation. (**C**) KEGG enrichment analysis of overlapping 63 DEGs between RNA-Seq and network pharmacology. (**D**) PPI network of 63 DEGs. Degree-based nodes were displayed. The node with a higher Degree value was expressed by the deeper color. (**E**) MCC-based top 15 DEGs in the PPI network. The node with the better centrality in the PPI network was expressed by the deeper color. (**F**) The relational network between key DEGs and inflammatory and apoptotic pathways.

QFHXD's anti-PF effect. Integrated analyses of the PPI network of 63 DEGs (Figure 5D), top 15 MCC-based targets (Figure 5E) and top 15 Degree-based DEGs (Supplementary Table S7) yielded novel pivotal DEGs (eg, TLR2, CCL2, SPP1, TNF, MMP13, and MMP14) for subsequent verification (Figure 5F).

https://doi.org/10.2147/DDDT.S592770

QFHXD Intervention Suppressed Inflammation in BLM-Induced PF Mice via the Regulation of Inflammatory Targets

To investigate the role of QFHXD in regulating inflammation to alleviate BLM-induced PF injury, we measured the expression of candidate inflammatory targets in biological samples from each group via RT-qPCR, immunohistochemistry, and ELISA. As expected, BLM stimulation triggered an anomalous augmentation of pro-inflammatory factors in the fibrotic lung tissues compared to the normal controls (Figure 6), as supported by inflammatory phenotypes observed in H&E staining and serum ELISA. However, continuous treatment with different doses of QFHXD reversed the aberrant mRNA levels of pro-inflammatory genes, including Tlr2, Tlr4, Rela, Nfkb1, Il1b, Il6, Tnf, Tgfb1, Ccl2, Spp1, Mmp9, Mmp13, and Mmp14, in BLM-exposed PF mice (Figure 6A and B). Consistently, QFHXD administration effectively reduced the pathological increase in protein contents of TLR2, TLR4, NF-κB, IL-1β, IL-6, TNF-α, TGF-β1, CCL2, and SPP1 in impaired lung tissues (Figure 6C–K). Additionally, immunohistochemical staining showed that administration of QFHXD at low and high doses markedly attenuated the exceptionally enhanced protein expression of matrix metallopeptidase 9 (MMP9) in the lung sections of PF mice (Figure 6L and M). These data jointly demonstrated the essential contribution of QFHXD's multi-target anti-inflammatory activity to its anti-PF efficacy.

QFHXD Intervention Modulated Apoptosis-Related Targets and Reduced Lung Apoptosis in BLM-Induced PF Mice

TUNEL staining of lung sections revealed a substantial increase in apoptotic cells (green color) in BLM-stimulated PF mice compared to the controls (Figure 7A and B). In contrast, high-dose QFHXD treatment prominently diminished the number of apoptotic cells (Figure 7A and B). RT-qPCR and immunohistochemistry results showed that BLM challenge led to dysregulated mRNA expression of anti-apoptotic gene (Bcl2) and pro-apoptotic genes (Bax and Casp3), as compared to those in the control group (Figure 7C–E). These changes were effectively reversed by QFHXD treatment, which significantly upregulated Bcl2 and downregulated Bax and Casp3 mRNA levels of PF mice (Figure 7C–E). Immunohistochemical analysis confirmed that QFHXD intervention significantly lowered the abnormally increased expression of Caspase-3 protein in lung sections of PF mice (Figure 7F and G). Together, these results suggested that QFHXD's anti-PF effect was partly mediated through multi-target modulation of anti-apoptotic mechanism.

Determination of Active Constituents in QFHXD Against BLM-Stimulated PF

Given the observed efficacy of QFHXD in improving BLM-stimulated PF phenotypes, we employed an integrated approach combining in vitro assays and molecular docking to identify its effective constituents. Immunofluorescence staining showed that TGF-β1 exposure markedly amplified the expression of pro-fibrotic markers (FN and Collagen I) in MRC-5 cells (Figure 8A–D). Conversely, similar to the TGF-β1 inhibitor SB-431542, QFHXD treatment obviously reduced FN and Collagen I expression, mirroring QFHXD's anti-PF action observed in vivo (Figure 8A–D). From 46 identified absorbable and lung-distributed compounds in QFHXD, 14 were selected for further screening. Compared with TGF-β1-stimulated MRC-5 cells without drug incubation, peimine and tanshinone IIA effectively downregulated FN protein expression (Figure 8E and F), whereas peiminine significantly decreased Collagen I protein expression (Figure 8G and H). Notably, loganin, baicalein, baicalin, oroxylin A, nobiletin, and paeoniflorin effectively normalized the abnormal expression of both FN and Collagen I induced by TGF-β1 stimulation (Figure 8E–H).

In addition, molecular docking results indicated that the binding energies between ligands (loganin, baicalein, baicalin, oroxylin A, peimine, peiminine, tanshinone IIA, nobiletin, and paeoniflorin) and receptors (TGF-β1, TLR4, CCL2, SPP1, MMP9, and Caspase-3) were all below −5 kcal/mol, highlighting their good affinity properties (Table 3 and Supplementary Figures S3–S5). Thus, these components represented the major anti-PF active constituents of QFHXD, functioning through multi-target regulation.

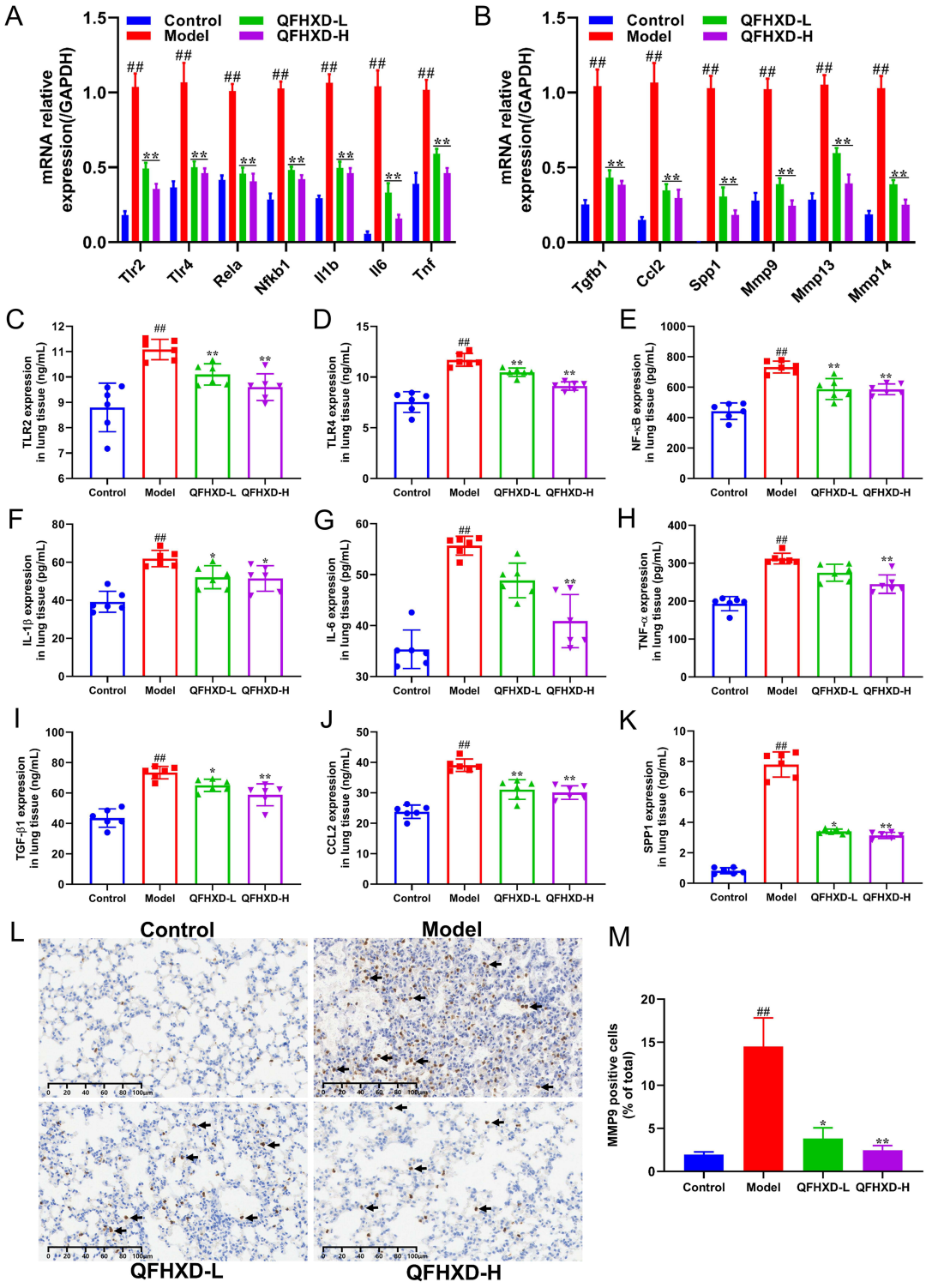

Figure 6 Experimental validation of inflammatory targets regulated by QFHXD in BLM-induced PF. (**A** and **B**) The relative mRNA levels of key inflammatory targets obtained from network pharmacology and RNA-Seq analysis, including Tlr2, Tlr4, Rela, Nfkb1, Il1b, Il6, Tnf, Tgfb1, Ccl2, Spp1, Mmp9, Mmp13, and Mmp14 (n = 5). The concentrations of TLR2 (**C**), TLR4 (**D**), NF-κB (**E**), IL-1β (**F**), IL-6 (**G**), TNF-α (**H**), TGF-β1 (**I**), CCL2 (**J**), and SPP1 (**K**) proteins were investigated by ELISA (n = 6). (**L**) The typical images of immunohistochemical staining of MMP9 protein in each group (×200 magnification, scale bar: 100 μm, n = 6). Black arrows indicated MMP9-positive cells. (**M**) Quantification of MMP9-positive cells (n = 6). Compared with the untreated PF model group, QFHXD intervention significantly suppressed the mRNA and protein expression of pro-inflammatory mediators in fibrotic lung samples. RT-qPCR results are expressed as the mean ± SEM. Data of ELISA and immunohistochemical staining are displayed as the mean ± SD. $^{\#\#}P < 0.01$ versus the control group; $^{*}P < 0.05$, and $^{**}P < 0.01$ versus the model group. Model, BLM-induced PF model; QFHXD-L, QFHXD low dose (4.78 g/kg); QFHXD-H, QFHXD high dose (9.56 g/kg).

https://doi.org/10.2147/DDDT.S592770

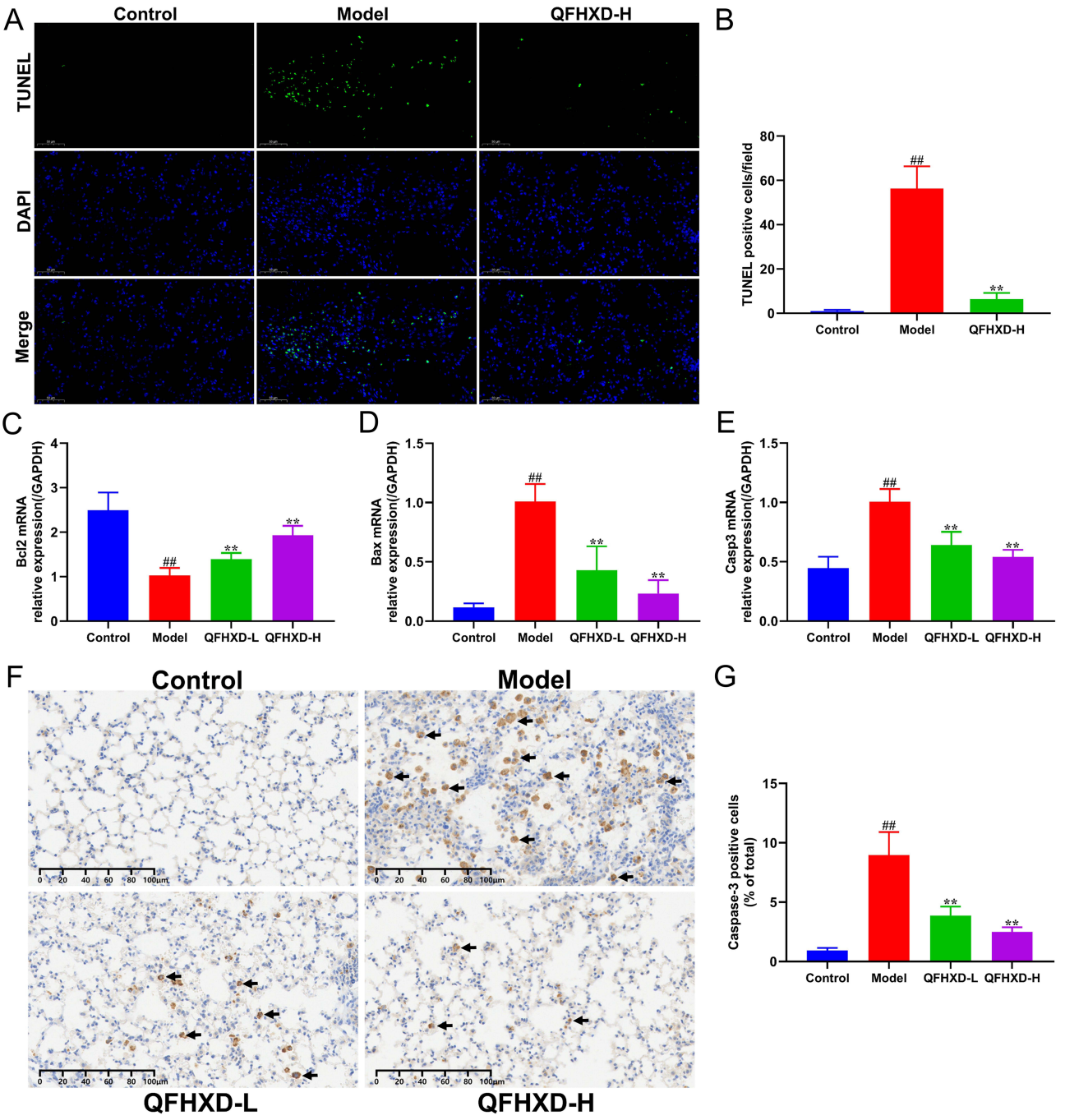

Figure 7 Investigation of anti-apoptotic mechanism of QFHXD in BLM-induced PF. (**A**) The typical images of cell apoptosis detected by TUNEL staining (×630 magnification, scale bar: 50 μm, n = 5). Green color represented TUNEL-positive cells, and blue color represented nuclei. (**B**) Quantification of TUNEL-positive cells in each group (n = 5). The relative mRNA levels of key apoptosis-related genes, including Bcl2 (**C**), Bax (**D**), and Casp3 (**E**) (n = 5). QFHXD treatment exhibited a positive anti-apoptotic activity in response to BLM-induced PF. (**F**) The representative immunohistochemical images of Caspase-3 protein expression in lung slices (×200 magnification, scale bar: 100 μm, n = 6). Caspase-3-positive cells were indicated by black arrows. (**G**) Quantitative analysis of Caspase-3 positive cells (n = 6). QFHXD treatment effectively normalized the dysregulated expression of Bcl2, Bax, and Caspase-3. Data are expressed as the mean ± SD. $^{\#\#}P < 0.01$ versus the control group; $^{**}P < 0.01$ versus the model group. Model, BLM-induced PF model; QFHXD-L, QFHXD low dose (4.78 g/kg); QFHXD-H, QFHXD high dose (9.56 g/kg).

Discussion

PF has emerged as a major global health challenge, characterized by significant symptom burden, unfavorable clinical outcomes, and restricted therapeutic options.[33] Alarmingly, the available evidence indicates that COVID-19 survivors face an elevated risk of PF as a post-infection sequela.[34,35] While monotherapy with pirfenidone or nintedanib remains a conditionally

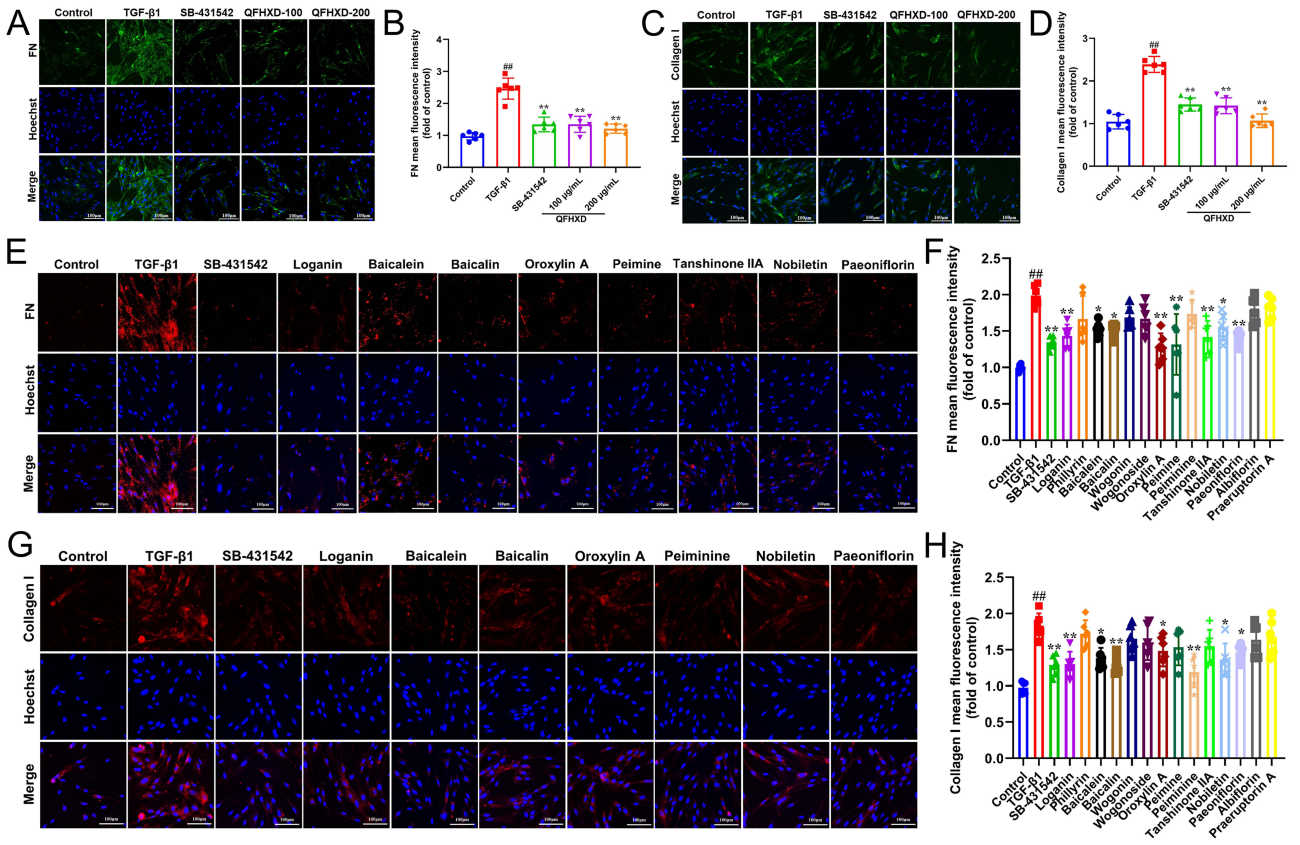

Figure 8 Screening for anti-PF active substances in QFHXD using immunofluorescence. (**A**) The representative immunofluorescence images of FN expression in TGF-β1-stimulated MRC-5 cells treated with QFHXD (×40 magnification, scale bar: 100 μm). (**B**) Quantitative analysis of FN protein expression regulated by QFHXD. (**C**) The representative immunofluorescence images of Collagen I expression in TGF-β1-stimulated MRC-5 cells treated with QFHXD (×40 magnification, scale bar: 100 μm). (**D**) Quantitative analysis of Collagen I protein expression regulated by QFHXD. (**E**) The typical immunofluorescence images of FN expression following incubation with anti-PF active components (×40 magnification, scale bar: 100 μm). (**F**) Quantification of FN protein levels in each group. (**G**) The typical immunofluorescence images of Collagen I expression following incubation with anti-PF active components (×40 magnification, scale bar: 100 μm). (**H**) Quantification of Collagen I protein levels in each group. Incubation with either loganin, baicalein, baicalin, oroxylin A, nobiletin, or paeoniflorin effectively rescued the abnormal expression of FN and Collagen I in TGF-β1-stimulated MRC-5 cells. Data are expressed as the mean ± SD from six independent experiments. $^{\#\#}P < 0.01$ versus the control group; $^{*}P < 0.05$, and $^{**}P < 0.01$ versus the TGF-β1 group.

recommended mainstay for PF, their associated side effects underscore the urgent need for novel anti-fibrotic strategies.[36] The accumulating pharmacological evidence indicates that TCM prescriptions, CMHs, and their active compounds combat PF through multi-channel regulation, such as inflammatory inhibition, oxidation resistance, reduction of ECM deposition, anti-

Table 3 Docking Scores of Anti-PF Active Constituents and PF-Related Key Target Proteins

Active Compounds	Binding Affinity with Hub Targets (kcal/mol)					
	TGF-β1	TLR4	CCL2	SPP1	MMP9	Caspase-3
Loganin	−5.7	−6.4	−5.4	−5.9	−6.7	−6.2
Baicalein	−6.8	−7.3	−5.9	−5.6	−7.8	−7.5
Baicalin	−7.0	−7.8	−6.2	−6.6	−7.6	−8.1
Oroxylin A	−6.2	−6.8	−5.6	−5.6	−6.3	−7.2
Peimine	−7.1	−7.5	−6.6	−7.3	−7.5	−8.3
Peiminine	−7.4	−7.8	−6.7	−7.3	−8.2	−8.4
Tanshinone IIA	−7.2	−7.9	−6.1	−6.4	−9.3	−7.4
Nobiletin	−5.8	−5.9	−5.3	−5.4	−6.1	−6.2
Paeoniflorin	−7.2	−7.4	−5.9	−6.3	−7.9	−7.1

https://doi.org/10.2147/DDDT.S592770

apoptosis, and suppression of epithelial-mesenchymal transition, thereby holding promising prospects for PF drug discovery.[14,37–39] QFHXD, an 18-herb formula, is clinically applied to treat lung disorders by clearing heat, expelling phlegm, promoting Qi, and activating blood.[15] Building on our prior finding that QFHXD ameliorated acute lung injury by modulating TLR4/NF-κB pathway-mediated inflammation,[15] the present study aimed to investigate its anti-PF efficacy, and to elucidate its potential regulatory mechanisms and anti-PF effective components.

The BLM-induced animal model is a well-established approach for modeling PF, as it effectively recapitulates key pathological features of the disease with high reproducibility and straightforward implementation.[23] PF is thought to originate from repeated alveolar epithelial damage, which drives fibroblast activation, myofibroblast differentiation, and excessive ECM deposition, ultimately resulting in alveolar destruction, lung dysfunction, and reduced survival.[40,41] In our study, a single intratracheal instillation of BLM successfully recapitulated the hallmarks of PF in treated mice over a 22-day period (Figure 1). The induced phenotypes encompassed histopathological lesions on H&E staining, alveolar epithelial injury (elevated serum KL-6), substantial ECM accumulation, as evidenced by Masson-stained collagen deposition and enhanced levels of α-SMA, FN, and collagen type I alpha 1 chain (COL1A1). Additionally, serum levels of TGF-β1 and CCL2 were elevated. These pathological changes collectively led to weight loss and increased mortality. Therapeutically, our results indicated that QFHXD treatment effectively improved histopathological features, body weight, and survival in PF mice. These benefits were associated with preserved alveolar integrity, inhibited inflammation, reduced expression of pro-fibrotic markers, and decreased ECM deposition (Figure 1). This study provided the first in vivo evidence that QFHXD has anti-PF efficacy, as demonstrated by multiple pharmacodynamic indicators.

Inflammation is believed to be an important contributor to the onset and progression of PF.[42,43] Damage to alveolar epithelial cells (AECs) triggers the secretion of diverse cytokines and chemokines, which in turn drive the recruitment and activation of immune cells (eg, neutrophils, macrophages, monocytes, and lymphocytes) to the injury site.[44] A persistent immune stimulation generates a hyper-inflammatory microenvironment, initiating a critical cascade of epithelial-mesenchymal transition, fibroblast activation, and subsequent formation of ECM-producing myofibroblasts, which ultimately accelerates PF progression.[45,46] Currently, anti-inflammatory strategy has emerged as a promising therapeutic approach for PF.[37,47] To elucidate the anti-PF mechanisms of QFHXD, we employed an integrated approach of network pharmacology and transcriptome sequencing. Enrichment analyses of the constructed component-target-disease network underlined a strong association between QFHXD's anti-PF activity and inflammation-related biological processes and signaling pathways, which was further corroborated by RNA-Seq analysis (Figures 4A, B and 5C). Through integrating the detailed analyses of network pharmacology and RNA-Seq, a series of candidate targets involved in inflammation, such as TGFB1, TLR2, TLR4, RELA, NFKB1, IL6, IL1B, TNF, CCL2, MMP9, and SPP1, were finally determined to disclose anti-inflammatory mechanism of QFHXD against PF (Figures 4C–E and 5D–F).

Numerous studies have established the critical role of TGF-β1 in the pathogenesis of PF.[48] As a pleiotropic pro-fibrotic mediator, TGF-β1 overexpression promotes chronic inflammation via the recruitment of immune cells and release of pro-inflammatory mediators, and drives the epithelial-mesenchymal transition, myofibroblast phenotypes, and ECM accumulation.[49,50] The heightened TGF-β1 levels have been consistently observed in both human subjects and animal models of PF.[51,52] Toll-like receptors (TLRs), particularly TLR2 and TLR4, are implicated in the pathophysiology of PF.[53] During BLM challenge, activated TLR2/TLR4 induces NF-κB signaling, leading to the production and secretion of pro-inflammatory cytokines (IL-1β, IL-6, and TNF-α), thereby activating inflammatory cascades and pro-fibrotic phenotypes.[54–56] As a pivotal chemokine, CCL2 not only mediates the chemotactic recruitment of immune cells (eg, monocytes and macrophages) to pathological sites and exacerbates inflammation, but also contributes to fibroblast activation and collagen production.[57] The enhanced expression of CCL2 is associated with an increased risk of adverse outcomes in PF patients.[58,59] MMP9, primarily secreted by AECs, macrophages, neutrophils, and fibroblasts, is upregulated in both animal models and patients with PF.[60,61] Its dysregulated activity promotes the migration of inflammatory cells, provokes the release of inflammatory mediators, and disrupts ECM homeostasis.[62] SPP1, a potential biomarker, is commonly highly expressed in PF patients with a poor prognosis.[63] In the context of PF, SPP1 acts as a multifunctional cytokine that regulates inflammation and fibrosis. Its upregulation stimulates macrophage-mediated inflammation and drives epithelial-mesenchymal transition along with fibroblast activation.[64,65] Consistently, our study demonstrated that QFHXD treatment normalized the heightened transcription and protein levels of these inflammatory mediators in BLM-stimulated PF mice (Figure 6), supporting its multi-target anti-inflammatory mechanism against PF.

Apoptosis, or programmed cell death, significantly contributes to the pathogenesis of PF.[66] In PF, the pathological amplification of apoptotic AECs impairs re-epithelialization and recruits fibroblasts to damaged sites, resulting in excessive ECM deposition.[67,68] In addition to the inflammatory mechanism, apoptosis-related biological processes and signaling pathways were also enriched (Figures 4A and B, 5C), pointing to apoptotic modulation in the anti-PF action of QFHXD. Consistent with this, high-dose QFHXD markedly attenuated pathological apoptosis in BLM-damaged lung tissues, as evidenced by TUNEL assay (Figure 7A and B), confirming its anti-apoptotic activity. The B-cell lymphoma-2 (Bcl-2) family proteins, which comprise anti-apoptotic and pro-apoptotic members, serve as crucial regulators of apoptosis and fibrosis.[69] The cellular susceptibility to apoptotic stimuli depends on the dynamic balance between the anti-apoptotic and pro-apoptotic molecules.[70] This balance is disrupted in epithelial cells of PF patients, manifested as decreased Bcl-2 and increased Bcl-2-associated X protein (Bax).[67] As a key executioner of apoptosis, Caspase-3 is activated through both extrinsic (death receptor-mediated) and intrinsic (mitochondria-mediated) pathways.[71] Its hyper-activation can trigger excessive apoptosis of alveolar cells, contributing to fibrogenesis.[72] Similarly, BLM stimulation led to dysregulated mRNA levels of Bcl2 and Bax, along with overexpression of Caspase-3 at both mRNA and protein levels in our study (Figure 7C–G). Fortunately, QFHXD intervention effectively normalized the expression of these apoptotic targets in BLM-induced PF mice (Figure 7C–G). These results revealed multi-target apoptotic modulation as a significant mechanism through which QFHXD inhibited BLM-induced PF.

TCM-based serum pharmacochemistry has demonstrated that the pharmacodynamic effects of TCM prescriptions are mediated by their absorbable components, including prototypes and metabolites.[73] Investigating the multi-component tissue distribution of TCM prescriptions can provide insight into the distribution patterns of bioactive components and illuminate their potential pharmacological activities.[74] Through integrating serum pharmacochemistry and lung tissue distribution analyses, this study identified 37 absorbable and 24 lung-distributed components of QFHXD in vivo (Figure 2, Table 1 and Table 2), suggesting their potential contribution to QFHXD's anti-PF efficacy. In TGF-β1-stimulated MRC-5 cells, treatment with either loganin, baicalein, baicalin, oroxylin A, peimine, peiminine, tanshinone IIA, nobiletin, or paeoniflorin effectively restored the aberrant expression of pro-fibrotic markers (FN and Collagen I) to varying degrees (Figure 8E–8H). These findings are corroborated by existing reports that highlight the anti-PF potential of these constituents.[20,75–79] Our docking results further confirmed the binding properties between these active compounds and PF-relevant target proteins (TGF-β1, TLR4, CCL2, SPP1, MMP9, and Caspase-3) (Table 3 and Supplementary Figure S3–S5). Here, we provide the first conclusive evidence that these compounds serve as primary anti-PF substances in QFHXD. Meanwhile, the identification of Jinyinhua (monarch herb)-derived loganin, Huangqin (monarch herb)-derived baicalein, baicalin, and oroxylin A, as well as Zhebeimu (minister herb)-derived peimine and peiminine, Danshen (minister herb)-derived tanshinone IIA, Chenpi (minister herb)-derived nobiletin, and Baishao (minister herb)-derived paeoniflorin, demonstrates the major contribution of both monarch and minister herbs to the anti-PF activity of QFHXD.

While this work systematically investigated the anti-PF efficacy, mechanisms, and active substances of QFHXD, certain limitations warrant attention. For example, in the BLM-induced PF animal model, factors such as the mode of BLM administration, intervention timing for medication, and partial reversibility of fibrotic lesions can influence the final outcome and clinical translation.[80,81] Hence, the clinical efficacy of QFHXD for PF treatment in a real-world setting merits further assessment. The anti-PF constituents identified in QFHXD warrant further in vivo investigation to characterize their pharmacokinetic profiles and pharmacological effects. The molecular targets of these constituents require further identification using advanced target discovery technologies.[82]

Conclusion

Overall, our study demonstrated for the first time that a prophylactic-plus-therapeutic regimen of QFHXD exerted beneficial effects against BLM-induced PF, partially through the regulation of multi-target mediated inflammatory and apoptotic mechanisms. QFHXD's anti-PF efficacy was attributed to several active constituents, including loganin, baicalein, baicalin, oroxylin A, peimine, peiminine, tanshinone IIA, nobiletin, and paeoniflorin. These findings provide a strong foundation for future clinical translation, paving the way for the development of QFHXD as a promising multi-targeting anti-fibrotic agent derived from herbal medicine.

Abbreviations

α-SMA, alpha-smooth muscle actin; AECs, alveolar epithelial cells; ANOVA, one-way analysis of variance; Bax, Bcl-2-associated X protein; Bcl-2, B-cell lymphoma-2; BLM, bleomycin; CCL2, chemokine (C-C motif) ligand 2; CMHs, Chinese medicinal herbs; COL1A1, collagen type I alpha 1 chain; COVID-19, Coronavirus Disease 2019; CTD, Comparative Toxicogenomics Database; DAB, 3,3'-Diaminobenzidine Tetrahydrochloride; DAVID, Database for Annotation, Visualization and Integration Discovery; DEGs, differentially expressed genes; ECM, extracellular matrix; ELISA, Enzyme-linked immunosorbent assay; ESI^+, positive electrospray ionization; ESI^-, negative electrospray ionization; FDA, Food and Drug Administration; FN, Fibronectin; FPKM, Fragments Per Kilobase of exon model per Million mapped fragments; GAPDH, glyceraldehyde-3-phosphate dehydrogenase; GO, Gene Ontology; H&E, Hematoxylin & Eosin; HESI, heated-electrospray ionization; HERB, high-throughput experiment- and reference-guided database of traditional Chinese medicine; IL-1β, interleukin-1 beta; IL-6, interleukin-6; KEGG, Kyoto Encyclopedia of Genes and Genomes; KL-6, Krebs von den Lungen-6; MCC, maximal clique centrality; MCODE, Molecular Complex Detection; MMP9, matrix metallopeptidase 9; MS, mass spectrometry; NF-κB, nuclear factor-kappa B; PF, pulmonary fibrosis; PPI, protein-protein interaction; QFHXD, Qingfei Huoxue decoction; RNA-Seq, Ribonucleic acid sequencing; RT-qPCR, Real-time quantitative polymerase chain reaction; SARS-CoV-2, Severe Acute Respiratory Syndrome Coronavirus 2; SD, Sprague Dawley; SPP1, secreted phosphoprotein 1; STRING, Search Tool for Recurring Instances of Neighboring Genes; TCM, traditional Chinsed medicine; TCMSP, Traditional Chinese Medicine Systems Pharmacology Database and Analysis Platform; TGF-β1, transforming growth factor-beta1; TLR2, toll-like receptor 2; TLR4, toll-like receptor 4; TLRs, toll-like receptors; TNF-α, tumor necrosis factor-alpha; TUNEL, Terminal Deoxynucleotidyl Transferase-mediated dUTP Nick-End Labeling; UPLC-Q-Orbitrap-MS/MS, ultra-high-performance liquid chromatography coupled with Q-Exactive quadrupole-orbitrap mass spectrometry.

Funding

This work was financially supported by grants from the Construction Fund of Key Medical Disciplines of Hangzhou (Grant No. 2025HZZD06), the Hangzhou Agricultural and Social Development Research Program (Grant No. 20231203A07), and the Medical and Health Technology Project of Hangzhou (Grant No. Z20240018). We appreciate OE Biotechnology Co., Ltd. (Shanghai, China) for the technical support of chemical profiling of QFHXD in vitro and vivo, and transcriptome sequencing.

Disclosure

The authors have no conflict of interest to declare.

References

1. Richeldi L, Collard HR, Jones MG. Idiopathic pulmonary fibrosis. *Lancet*. 2017;389(10082):1941–1952. doi:10.1016/S0140-6736(17)30866-8
2. Spagnolo P, Kropski JA, Jones MG, et al. Idiopathic pulmonary fibrosis: disease mechanisms and drug development. *Pharmacol Ther*. 2021;222:107798. doi:10.1016/j.pharmthera.2020.107798
3. Moss BJ, Ryter SW, Rosas IO. Pathogenic mechanisms underlying idiopathic pulmonary fibrosis. *Annu Rev Pathol*. 2022;17(1):515–546. doi:10.1146/annurev-pathol-042320-030240
4. Naqvi M, Hannah J, Lawrence A, et al. Antifibrotic therapy in progressive pulmonary fibrosis: a review of recent advances. *Expert Rev Respir Med*. 2024;18(6):397–407. doi:10.1080/17476348.2024.2375420
5. Alrajhi NN. Post-COVID-19 pulmonary fibrosis: an ongoing concern. *Ann Thorac Med*. 2023;18(4):173–181. doi:10.4103/atm.atm_7_23
6. John AE, Joseph C, Jenkins G, et al. COVID-19 and pulmonary fibrosis: a potential role for lung epithelial cells and fibroblasts. *Immunol Rev*. 2021;302(1):228–240. doi:10.1111/imr.12977
7. Hujjat SFZ, Chandani HK, Chandani DK, et al. Jascayd (nerandomilast): a novel PDE4B inhibitor for idiopathic pulmonary fibrosis. *Ann Med Surg Lond*. 2025;88(1):1–4. doi:10.1097/MS9.0000000000004290
8. Keith R, Nambiar AM. Potential of phosphodiesterase 4B inhibition in the treatment of progressive pulmonary fibrosis. *Ther Adv Respir Dis*. 2025;19:17534666241309795. doi:10.1177/17534666241309795
9. He M, Yang T, Zhou J, et al. A real-world study of antifibrotic drugs-related adverse events based on the United States food and drug administration adverse event reporting system and VigiAccess databases. *Front Pharmacol*. 2024;15:1310286. doi:10.3389/fphar.2024.1310286
10. Podolanczuk AJ, Thomson CC, Remy-Jardin M, et al. Idiopathic pulmonary fibrosis: state of the art for 2023. *Eur Respir J*. 2023;61(4):2200957. doi:10.1183/13993003.00957-2022
11. Hao Y, Li J, Dan L, et al. Chinese medicine as a therapeutic option for pulmonary fibrosis: clinical efficacies and underlying mechanisms. *J Ethnopharmacol*. 2024;318(Pt A):116836. doi:10.1016/j.jep.2023.116836

12. Ji K, Ma J, Wang L, et al. Efficacy and safety of traditional Chinese medicine in idiopathic pulmonary fibrosis: a meta-analysis. *Evid Based Complement Alternat Med*. 2020;2020(1):1752387. doi:10.1155/2020/1752387
13. Sun WY, Zhang XQ, Guo YJ, et al. Evidence mapping analysis of traditional Chinese medicine intervention in pulmonary fibrosis. *Zhongguo Zhong Yao Za Zhi*. 2023;48(20):5641–5650. Chinese. doi:10.19540/j.cnki.cjcmm.20230618.501
14. Zhou YM, Dong XR, Xu D, et al. Therapeutic potential of traditional Chinese medicine for interstitial lung disease. *J Ethnopharmacol*. 2024;318(Pt A):116952. doi:10.1016/j.jep.2023.116952
15. Wang Y, Li B, Zhang Y, et al. Qingfei Huoxue decoction and its active component narirutin alleviate LPS-induced acute lung injury by regulating TLR4/NF-κB pathway mediated inflammation. *J Inflamm Res*. 2024;17:7503–7520. doi:10.2147/JIR.S480101
16. Lee HL, Kim JM, Go MJ, et al. Protective effect of *Lonicera japonica* on PM2.5-induced pulmonary damage in BALB/c mice via the TGF-β and NF-κB pathway. *Antioxidants*. 2023;12(4):968. doi:10.3390/antiox12040968
17. Wang D, Li Y. Pharmacological effects of baicalin in lung diseases. *Front Pharmacol*. 2023;14:1188202. doi:10.3389/fphar.2023.1188202
18. Wu Q, Zhou Y, Zhou XM. Citrus alkaline extract delayed the progression of pulmonary fibrosis by inhibiting p38/NF-κB signaling pathway-induced cell apoptosis. *Evid Based Complement Alternat Med*. 2019;2019:1528586. doi:10.1155/2019/1528586
19. Xu Y, Wang X, Han D, et al. Revealing the mechanism of Jiegeng decoction attenuates bleomycin-induced pulmonary fibrosis via PI3K/Akt signaling pathway based on lipidomics and transcriptomics. *Phytomedicine*. 2022;102:154207. doi:10.1016/j.phymed.2022.154207
20. Qin Y, Yang J, Li H, et al. Recent advances in the therapeutic potential of nobiletin against respiratory diseases. *Phytomedicine*. 2024;128:155506. doi:10.1016/j.phymed.2024.155506
21. Zhi X, Ren C, Li Q, et al. Therapeutic potential of *Angelica sinensis* in addressing organ fibrosis: a comprehensive review. *Biomed Pharmacother*. 2024;173:116429. doi:10.1016/j.biopha.2024.116429
22. Huang P, Wang X, Cao Y, et al. Research progress on the use of *Salvia miltiorrhiza* Bunge extracts in the treatment of pulmonary diseases. *Biomed Pharmacother*. 2024;179:117282. doi:10.1016/j.biopha.2024.117282
23. Liu T, De Los Santos FG, Phan SH. The bleomycin model of pulmonary fibrosis. *Methods Mol Biol*. 2017;1627:27–42. doi:10.1007/978-1-4939-7113-8_2
24. Ashcroft T, Simpson JM, Timbrell V. Simple method of estimating severity of pulmonary fibrosis on a numerical scale. *J Clin Pathol*. 1988;41(4):467–470. doi:10.1136/jcp.41.4.467
25. Wang Y, Wu H, Han Z, et al. Guhong injection promotes post-stroke functional recovery via attenuating cortical inflammation and apoptosis in subacute stage of ischemic stroke. *Phytomedicine*. 2022;99:154034. doi:10.1016/j.phymed.2022.154034
26. Guo X, Wu Y, Wang Q, et al. Huperzine A injection ameliorates motor and cognitive abnormalities via regulating multiple pathways in a murine model of Parkinson's disease. *Eur J Pharmacol*. 2023;956:175970. doi:10.1016/j.ejphar.2023.175970
27. Fang S, Dong L, Liu L, et al. HERB: a high-throughput experiment- and reference-guided database of traditional Chinese medicine. *Nucleic Acids Res*. 2021;49(D1):D1197–D1206. doi:10.1093/nar/gkaa1063
28. Ru J, Li P, Wang J, et al. TCMSP: a database of systems pharmacology for drug discovery from herbal medicines. *J Cheminform*. 2014;6(1):13. doi:10.1186/1758-2946-6-13
29. Chen T, Liu YX, Chen T, et al. ImageGP 2 for enhanced data visualization and reproducible analysis in biomedical research. *Imeta*. 2024;3(5):e239. doi:10.1002/imt2.239
30. Bader GD, Hogue CW. An automated method for finding molecular complexes in large protein interaction networks. *BMC Bioinf*. 2003;4(1):2. doi:10.1186/1471-2105-4-2
31. Chin CH, Chen SH, Wu HH, et al. cytoHubba: identifying hub objects and sub-networks from complex interactome. *BMC Syst Biol*. 2014;8 Suppl 4 (Suppl 4):S11. doi:10.1186/1752-0509-8-S4-S11
32. Love MI, Huber W, Anders S. Moderated estimation of fold change and dispersion for RNA-seq data with DESeq2. *Genome Biol*. 2014;15(12):550. doi:10.1186/s13059-014-0550-8
33. Cheng W, Zeng Y, Wang D. Stem cell-based therapy for pulmonary fibrosis. *Stem Cell Res Ther*. 2022;13(1):492. doi:10.1186/s13287-022-03181-8
34. Hirawat R, Jain N, Aslam Saifi M, et al. Lung fibrosis: post-COVID-19 complications and evidences. *Int Immunopharmacol*. 2023;116:109418. doi:10.1016/j.intimp.2022.109418
35. George PM, Wells AU, Jenkins RG. Pulmonary fibrosis and COVID-19: the potential role for antifibrotic therapy. *Lancet Respir Med*. 2020;8(8):807–815. doi:10.1016/S2213-2600(20)30225-3
36. Chianese M, Screm G, Salton F, et al. Pirfenidone and nintedanib in pulmonary fibrosis: lights and shadows. *Pharmaceuticals*. 2024;17(6):709. doi:10.3390/ph17060709
37. Qin S, Tan P, Xie J, et al. A systematic review of the research progress of traditional Chinese medicine against pulmonary fibrosis: from a pharmacological perspective. *Chin Med*. 2023;18(1):96. doi:10.1186/s13020-023-00797-7
38. Hosseini S, Imenshahidi M, Hosseinzadeh H, et al. Effects of plant extracts and bioactive compounds on attenuation of bleomycin-induced pulmonary fibrosis. *Biomed Pharmacother*. 2018;107:1454–1465. doi:10.1016/j.biopha.2018.08.111
39. Wang Q, Li W, Hu H, et al. Monomeric compounds from traditional Chinese medicine: new hopes for drug discovery in pulmonary fibrosis. *Biomed Pharmacother*. 2023;159:114226. doi:10.1016/j.biopha.2023.114226
40. Mei Q, Liu Z, Zuo H, et al. Idiopathic pulmonary fibrosis: an update on pathogenesis. *Front Pharmacol*. 2022;12:797292. doi:10.3389/fphar.2021.797292
41. Muri J, Durcova B, Slivka R, et al. Idiopathic pulmonary fibrosis: review of current knowledge. *Physiol Res*. 2024;73(4):487–497. doi:10.33549/physiolres.935322
42. Fathimath Muneesa M, Shaikh SB, Jeena TM, et al. Inflammatory mediators in various molecular pathways involved in the development of pulmonary fibrosis. *Int Immunopharmacol*. 2021;96:107608. doi:10.1016/j.intimp.2021.107608
43. Heukels P, Moor CC, von der Thusen JH, et al. Inflammation and immunity in IPF pathogenesis and treatment. *Respir Med*. 2019;147:79–91. doi:10.1016/j.rmed.2018.12.015
44. Burgoyne RA, Fisher AJ, Borthwick LA. The role of epithelial damage in the pulmonary immune response. *Cells*. 2021;10(10):2763. doi:10.3390/cells10102763
45. Phan THG, Paliogiannis P, Nasrallah GK, et al. Emerging cellular and molecular determinants of idiopathic pulmonary fibrosis. *Cell Mol Life Sci*. 2021;78(5):2031–2057. doi:10.1007/s00018-020-03693-7

46. Wynn TA. Integrating mechanisms of pulmonary fibrosis. *J Exp Med*. 2011;208(7):1339–1350. doi:10.1084/jem.20110551
47. Mutsaers SE, Miles T, Prele CM, et al. Emerging role of immune cells as drivers of pulmonary fibrosis. *Pharmacol Ther*. 2023;252:108562. doi:10.1016/j.pharmthera.2023.108562
48. Ye Z, Hu Y. TGF-β1: gentlemanly orchestrator in idiopathic pulmonary fibrosis (Review). *Int J Mol Med*. 2021;48(1):132. doi:10.3892/ijmm.2021.4965
49. Kang HR, Lee JY, Lee CG. TGF-β1 as a therapeutic target for pulmonary fibrosis and COPD. *Expert Rev Clin Pharmacol*. 2008;1(4):547–558. doi:10.1586/17512433.1.4.547
50. Peng D, Fu M, Wang M, et al. Targeting TGF-β signal transduction for fibrosis and cancer therapy. *Mol Cancer*. 2022;21(1):104. doi:10.1186/s12943-022-01569-x
51. Gul A, Yang F, Xie C, et al. Pulmonary fibrosis model of mice induced by different administration methods of bleomycin. *BMC Pulm Med*. 2023;23(1):91. doi:10.1186/s12890-023-02349-z
52. Zhang Y, Bi L, Qiu Y, et al. Elevated sL1-CAM levels in BALF and serum of IPF patients. *Respirology*. 2016;21(1):143–148. doi:10.1111/resp.12659
53. Karampitsakos T, Woolard T, Bouros D, et al. Toll-like receptors in the pathogenesis of pulmonary fibrosis. *Eur J Pharmacol*. 2017;808:35–43. doi:10.1016/j.ejphar.2016.06.045
54. Bolourani S, Brenner M, Wang P. The interplay of DAMPs, TLR4, and proinflammatory cytokines in pulmonary fibrosis. *J Mol Med*. 2021;99(10):1373–1384. doi:10.1007/s00109-021-02113-y
55. Razonable RR, Henault M, Paya CV. Stimulation of toll-like receptor 2 with bleomycin results in cellular activation and secretion of pro-inflammatory cytokines and chemokines. *Toxicol Appl Pharmacol*. 2006;210(3):181–189. doi:10.1016/j.taap.2005.05.002
56. Wei Y, Qi M, Liu C, et al. Astragalus polysaccharide attenuates bleomycin-induced pulmonary fibrosis by inhibiting TLR4/NF-κB signaling pathway and regulating gut microbiota. *Eur J Pharmacol*. 2023;944:175594. doi:10.1016/j.ejphar.2023.175594
57. Liu S, Liu C, Wang Q, et al. CC Chemokines in idiopathic pulmonary fibrosis: pathogenic role and therapeutic potential. *Biomolecules*. 2023;13(2):333. doi:10.3390/biom13020333
58. Gui X, Qiu X, Tian Y, et al. Prognostic value of IFN-γ, sCD163, CCL2 and CXCL10 involved in acute exacerbation of idiopathic pulmonary fibrosis. *Int Immunopharmacol*. 2019;70:208–215. doi:10.1016/j.intimp.2019.02.039
59. Shinoda H, Tasaka S, Fujishima S, et al. Elevated CC chemokine level in bronchoalveolar lavage fluid is predictive of a poor outcome of idiopathic pulmonary fibrosis. *Respiration*. 2009;78(3):285–292. doi:10.1159/000207617
60. Pardo A, Cabrera S, Maldonado M, et al. Role of matrix metalloproteinases in the pathogenesis of idiopathic pulmonary fibrosis. *Respir Res*. 2016;17(1):23. doi:10.1186/s12931-016-0343-6
61. Zhao L, Mu B, Zhou R, et al. Iguratimod ameliorates bleomycin-induced alveolar inflammation and pulmonary fibrosis in mice by suppressing expression of matrix metalloproteinase-9. *Int J Rheum Dis*. 2019;22(4):686–694. doi:10.1111/1756-185X.13463
62. Bormann T, Maus R, Stolper J, et al. Role of matrix metalloprotease-2 and MMP-9 in experimental lung fibrosis in mice. *Respir Res*. 2022;23(1):180. doi:10.1186/s12931-022-02105-7
63. Liao Y, Wang R, Wen F. Diagnostic and prognostic value of secreted phosphoprotein 1 for idiopathic pulmonary fibrosis: a systematic review and meta-analysis. *Biomarkers*. 2023;28(1):87–96. doi:10.1080/1354750X.2022.2148744
64. Hatipoglu OF, Uctepe E, Opoku G, et al. Osteopontin silencing attenuates bleomycin-induced murine pulmonary fibrosis by regulating epithelial-mesenchymal transition. *Biomed Pharmacother*. 2021;139:111633. doi:10.1016/j.biopha.2021.111633
65. Hu W, Xu Y. Transcriptomics in idiopathic pulmonary fibrosis unveiled: a new perspective from differentially expressed genes to therapeutic targets. *Front Immunol*. 2024;15:1375171. doi:10.3389/fimmu.2024.1375171
66. Drakopanagiotakis F, Xifteri A, Polychronopoulos V, et al. Apoptosis in lung injury and fibrosis. *Eur Respir J*. 2008;32(6):1631–1638. doi:10.1183/09031936.00176807
67. Plataki M, Koutsopoulos AV, Darivianaki K, et al. Expression of apoptotic and antiapoptotic markers in epithelial cells in idiopathic pulmonary fibrosis. *Chest*. 2005;127(1):266–274. doi:10.1378/chest.127.1.266
68. Wang Q, Xie ZL, Wu Q, et al. Role of various imbalances centered on alveolar epithelial cell/fibroblast apoptosis imbalance in the pathogenesis of idiopathic pulmonary fibrosis. *Chin Med J*. 2021;134(3):261–274. doi:10.1097/CM9.0000000000001288
69. Safaeian L, Abed A, Vaseghi G. The role of Bcl-2 family proteins in pulmonary fibrosis. *Eur J Pharmacol*. 2014;741:281–289. doi:10.1016/j.ejphar.2014.07.029
70. Siddiqui WA, Ahad A, Ahsan H. The mystery of BCL2 family: bcl-2 proteins and apoptosis: an update. *Arch Toxicol*. 2015;89(3):289–317. doi:10.1007/s00204-014-1448-7
71. Asadi M, Taghizadeh S, Kaviani E, et al. Caspase-3: structure, function, and biotechnological aspects. *Biotechnol Appl Biochem*. 2022;69(4):1633–1645. doi:10.1002/bab.2233
72. Kuwano K, Hagimoto N, Nakanishi Y. The role of apoptosis in pulmonary fibrosis. *Histol Histopathol*. 2004;19(3):867–881. doi:10.14670/HH-19.867
73. Li S, Liu H, Zhang C, et al. Serum pharmacochemistry and pharmacokinetics of major components after oral administration of Luhong recipe in rats using ultra-performance liquid chromatography-tandem mass spectrometry. *Biomed Chromatogr*. 2022;36(12):e5497. doi:10.1002/bmc.5497
74. Zhuang G, Wang YQ, Li SJ, et al. Tissue distribution and molecular docking research on the active components of Bidens bipinnata L. against hyperlipidemia. *Biomed Chromatogr*. 2021;35(4):e5026. doi:10.1002/bmc.5026
75. Cai ZH, Tian YG, Li JZ, et al. Peimine ameliorates pulmonary fibrosis via the inhibition of M2-type macrophage polarization through the suppression of P38/Akt/STAT6 signals. *Biosci Rep*. 2022;42(10):BSR20220986. doi:10.1042/BSR20220986
76. Chen L, Ma Q, Zhang G, et al. Protective effect and mechanism of loganin and morroniside on acute lung injury and pulmonary fibrosis. *Phytomedicine*. 2022;99:154030. doi:10.1016/j.phymed.2022.154030
77. Guo H, Ji F, Liu B, et al. Peiminine ameliorates bleomycin-induced acute lung injury in rats. *Mol Med Rep*. 2013;7(4):1103–1110. doi:10.3892/mmr.2013.1312
78. Li LC, Kan LD. Traditional Chinese medicine for pulmonary fibrosis therapy: progress and future prospects. *J Ethnopharmacol*. 2017;198:45–63. doi:10.1016/j.jep.2016.12.042

79. Sharma A, Wairkar S. Flavonoids for treating pulmonary fibrosis: present status and future prospects. *Phytother Res*. 2024;38(9):4406–4423. doi:10.1002/ptr.8285
80. Della Latta V, Cecchettini A, Del Ry S, et al. Bleomycin in the setting of lung fibrosis induction: from biological mechanisms to counteractions. *Pharmacol Res*. 2015;97:122–130. doi:10.1016/j.phrs.2015.04.012
81. Kolb P, Upagupta C, Vierhout M, et al. The importance of interventional timing in the bleomycin model of pulmonary fibrosis. *Eur Respir J*. 2020;55(6):1901105. doi:10.1183/13993003.01105-2019
82. Yan S, Zhang G, Luo W, et al. PROTAC technology: from drug development to probe technology for target deconvolution. *Eur J Med Chem*. 2024;276:116725. doi:10.1016/j.ejmech.2024.116725